JURASSIC TO EARLY CRETACEOUS CRUSTAL THICKNESS IN THE COLOMBIAN NORTHERN ANDES: INSIGHT INTO THE MAGMATIC THERMAL VARIATIONS AND EMPLACEMENT CONDITIONS OF PLUTONIC ROCKS

Por

Luisa Fernanda Chavarría Chavarría

Asesor

Camilo Bustamante Londoño

Manuscrito requerido para optar al grado en

MAESTRÍA EN CIENCIAS DE LA TIERRA

DEPARTAMENTO DE CIENCIAS DE LA TIERRA

ESCUELA DE CIENCIAS

UNIVERSIDAD EAFIT

Resumen

En este estudio caracterizamos las variaciones en el espesor cortical y el flujo de fluidos magmáticos durante el Jurásico Temprano a Cretácico Temprano (194-130 Ma) en el arco asociado a subducción en los Andes del Norte en la Cordillera Central. Para esto usamos elementos traza, temperaturas de saturación en circón y apatito e isótopos de Sr-Nd. Adicionalmente, analizamos las implicaciones de las condiciones de emplazamiento durante la última etapa del magmatismo (165-130 Ma) aplicando termobarometría de Al en hornblenda y química mineral. Pendientes moderadas en los elementos de las tierras raras (ETR) y ETR pesadas más empobrecidas muestran que la fuente primaria del magma residual fue el anfíbol, sin embargo, la plagioclasa y el piroxeno también pudieron haber sido fases residuales importantes que indican que la fuente del magma se formó en una corteza que varió entre 35-50 km de espesor. Las variaciones de los cálculos cuantitativos del espesor cortical usando las razones de La/Yb y Sr/Y indican que el arco experimentó dos episodios de engrosamiento durante los periodos de 190 a 180 Ma y 165 a 154 Ma. El primer episodio está asociado con *underplating* basáltico durante una subducción de *slab rollback*. El último episodio de engrosamiento está relacionado con el cambio a una configuración de subducción oblicua con un posterior evento colisional que produjo rocas metamórficas de media P-T. Durante este periodo, los flujos de fluidos y los volúmenes magmáticos empezaron a disminuir progresivamente como es evidenciado por las temperaturas de saturación. Posteriormente, durante el Jurásico Tardío al Cretácico Temprano (154-130 Ma) la corteza se volvió más delgada y en este escenario se emplazó la última etapa del magmatismo. Las profundidades de emplazamiento variaron de niveles corticales someros a profundos y ocurrieron procesos magmáticos como deformación en estado sólido, inyección de pulsos máficos, mingling, y mezcla de diferentes etapas de cristalización magmática.

Jurassic to Early Cretaceous crustal thickness in the Colombian Northern Andes: Insight into the magmatic thermal variations and emplacement conditions of plutonic rocks

Luisa Chavarría

Abstract

We characterized the crustal thickness variations and magmatic fluid-fluxes of the Early Jurassic to Early Cretaceous (194-130 Ma) in plutonic rocks in the Central Cordillera of Colombia (Northern Andes) combining trace elements signatures, zircon and apatite saturation temperatures, and Sr-Nd isotopes. Additionally, we analyzed the implications of the emplacement conditions during the last stage of the magmatism (165-130 Ma) using Al-in-hornblende thermobarometry and mineral chemistry. Moderate rare earth elements (REE) slopes and depleted heavy REE patterns show that the primary residual magma source was amphibole, but plagioclase and pyroxene were also significant residual phases indicating that the magma source was formed in a crust that varied in thickness from 35-50 km. The variations of the La/Yb and Sr/Y crustal quantifications indicate that the arc underwent two thickening episodes during the 190 to 180 Ma and 165 to 154 Ma periods. The first episode is associated with basaltic underplating during slab rollback subduction. The last thickening episode is related to the shift to an oblique subduction setting, and a subsequent collisional event that produced medium P-T metamorphic rocks. During this period, the fluid fluxes and the magmatic volumes began to decrease progressively as the saturation temperatures record. Afterward, during the Late Jurassic to Early Cretaceous (154-130 Ma), the crust became thinner and, in this scenario, was emplaced the last stage of plutonism. Emplacement depths varied from shallow to deep levels in the crust and magmatic processes such as solid-state deformation, injection of mafic pulses, mingling and mixing of different crystallization magmatic stages occurred.

Keywords: Jurassic, Crustal thickness, Magmatism, Northern Andes, Emplacement

1. Introduction

Continental arcs form in subduction zones when an oceanic slab subducts beneath a continental lithosphere producing partial melts from the mantle wedge as a result of the dehydration of the oceanic crust. This interaction is one possible scenario for the formation of voluminous (>100 km^2) calc-alkaline batholiths that may last for tens to a hundred million years (Stern, 2002; Ducea et al., 2015; Collins et al., 2016). Their chemical and mineralogical composition, as well as their emplacement mechanism in the upper crust, give clues about the thermal and fluid flux in the subduction zones and can provide valuable information on the dynamics of subduction evolution through time, such as the slab dip and convergence velocity, sediment input of the subducting slab and source evolution (De Saint Blanquat et al., 1998; Stern, 2002; Matzel et al., 2006; Ji et al., 2014; Li et al., 2014; Ducea et al., 2015; Farner and Lee, 2017). Some of these variables (e.g., slab dip and convergence velocity) may also influence the rates of magma production and the extensional or compressional behavior of the arc that, in turn, determines changes in the crustal thickness (Ducea et al., 2015). When the arc is under compression, a low-angle slab dip reduces the amount of magma production, and crustal thicknesses may reach ca. 70 km (Stern, 2002; Ducea et al., 2015) such as in the Central Andes (Mamani et al., 2010; Wörner et al., 2018). On the other hand, during extension, the upper plate experiences basin formation, a thin-crust is formed (< 30 km) and is characterized by a high-angle of subduction (Stern, 2002; Ducea et al., 2015).

Although the Andes has been traditionally considered the natural laboratory for studying phases of crustal growth and arc magmatism in continental margins, the northern section of the Andean orogeny and its different Meso-Cenozoic magmatic phases remains less-well understood. In particular, the Jurassic magmatic arc of the Northern Andes (recorded from La Guajira at northern Colombia to southern Ecuador) registers a complex history that follows the fragmentation of Pangea at the end of the Triassic and the beginning of a new subduction zone in the Jurassic located at the western margin of South America (Ramos, 2009; Spikings et al., 2015; Bustamante et al., 2016; Rodríguez et al., 2018; Leal-Mejía et al., 2019). This Mesozoic setting allowed the formation of a long-lived magmatic arc in Colombia from ca. 200 to 129 Ma (Bustamante et al., 2016) characterized by a segmented

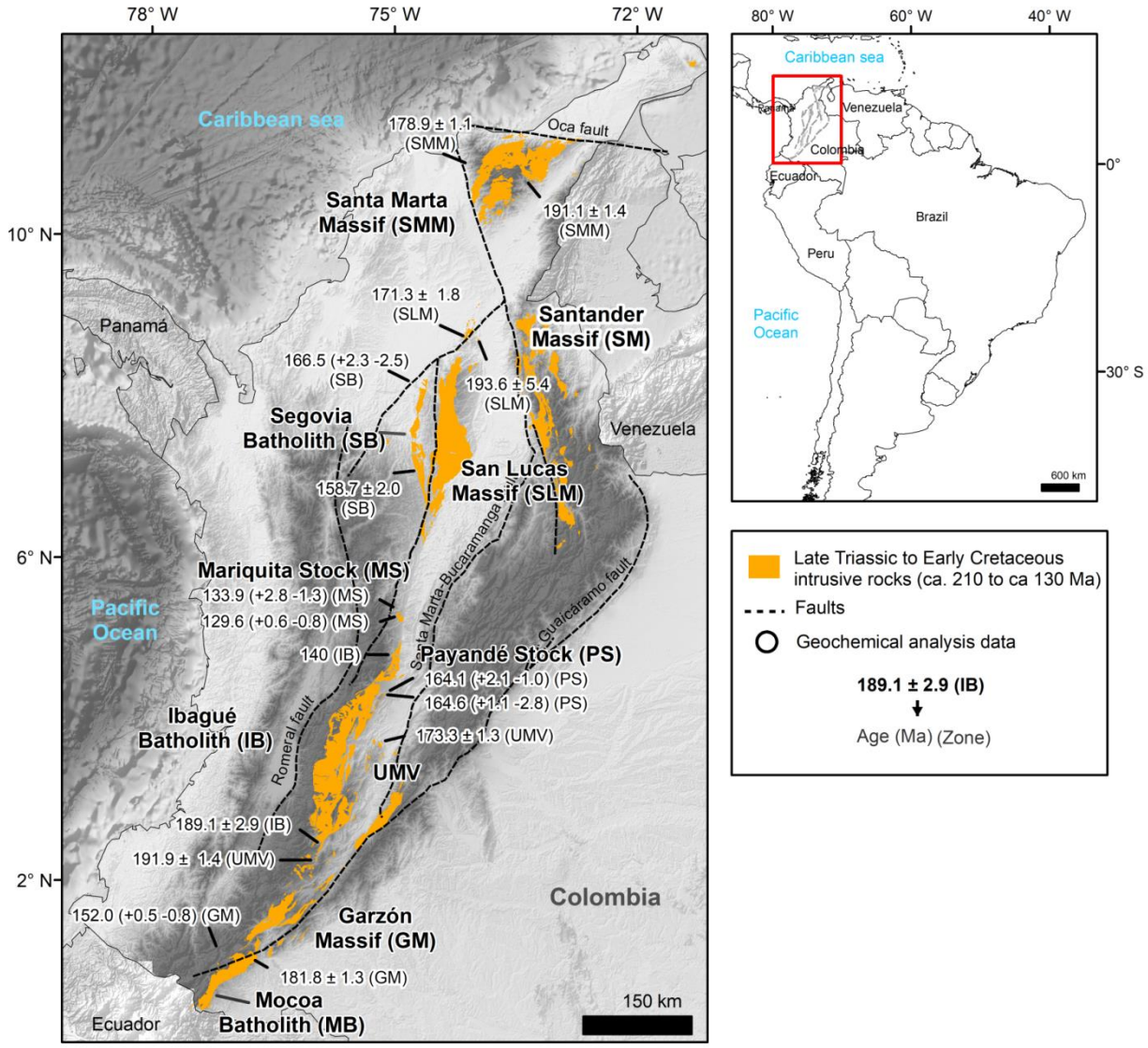

Figure 1. Distribution of the Jurassic to Early Cretaceous plutonic belt in the Northern Andes in Colombia. The map is showing the plutons grouped in geographic zones: Santa Marta Massif (SMM), Segovia Batholith (SB), San Lucas Massif (SLM), Santander Massif (SM), Mariquita Stock (MS), Payandé Stock (PS), Ibagué Batholith (IB), Upper Magdalena Valley (UMV) and Garzón Massif (GM). The minimum and maximum ages are zircon U-Pb geochronological data of the studied zones compiled from different authors. The white dots represent the locations where compiled whole-rock geochemical data is available. Compiled data is available in Supplementary Data Table 1.

belt of calc-alkaline granitic intrusions, extending for almost 1000 km in a NE direction from the Mocoa batholith in southern Colombia to the Sierra Nevada de Santa Marta in the north (Figure 1). Apparent changes in magma volumes through the Jurassic have been inferred from the areal distribution of the plutonic rocks and detrital zircon ages density from boreholes (Bustamante et al., 2016), and they revealed that the magmatic activity decreased from ~170 to 130 Ma, possibly related to variations in the convergence angles between the Farallon plate and NW South America (Bustamante et al., 2016; Quandt et al., 2018).

Currently, four scenarios with specific main controlling factors have been proposed to explain the evolution of the Jurassic magmatic arc: i) a rifting during the Triassic until the Late Jurassic (Cediel et al., 2003); ii) a slab-roll back from ca. 193 to 145 Ma, which causes back-arc extension, crustal thinning, and isotopically juvenile magmas (Cochrane et al., 2014; Spikings et al., 2015, 2019; Leal-Mejía et al., 2019); iii) oblique subduction from 170 to 130 Ma (Bustamante et al., 2016) that may also induce crustal thickening (De Saint Blanquat et al., 1998; Li et al., 2014); and iv) subduction erosion (Rodríguez et al., 2018). These contrasting models have direct implications in the crustal evolution of the arc and the emplacement conditions of the granitoid intrusives.

Most of the research carried on the Jurassic arc has been focused on petrographic, geochemical, and geochronological characterizations and limited to discuss the regional geological model. In contrast, the evaluation of the crustal thickness variations and thermal aspects associated with the arc evolution is still unclear, despite their importance for the generation and modification of the magmas. In this contribution, we analyze crustal thickness characteristics and temperature (crystallization and saturation) variations from the Jurassic to Early Cretaceous (194-130 Ma) rocks of the Central Cordillera of Colombia, seeking to evaluate the possible relations with the proposed model of oblique convergence or slab rollback regime in the evolution of the continental crust in the Northern Andes. We accomplished this by reviewing published geochronological, geochemical, and isotopic data in order to analyze REE ratios and patterns, Sr-Nd isotopic variations, and estimate zircon and apatite saturation temperatures of the plutonic rocks along the arc. Additionally,

in a more local approach, new mineral chemistry, thermobarometric analyses, and new Sr isotopic data are presented for selected plutons, representative of the southern segment of the Jurassic arc-related magmatism (Figure 2).

With a regional approach, we aim to (i) estimate the crustal thickness variations of the Jurassic arc and (ii) analyze the relationship between saturation temperatures and fluid fluxes of the remnants in the Santa Marta Massif, Central Cordillera and the Upper Magdalena Valley (latitude ~11°N to ~1°N) from ca. 194 to 130 Ma. Furthermore, in a local approach, we aim to (iii) determinate the emplacement conditions of the magma during the final stages of the arc magmatism in the southern part of the Central Cordillera when the volumes begin to decrease (ca. 165 to 130 Ma).

2. Geological setting

The Northern Andes, including Colombia and Ecuador, is divided into three sub-parallel mountain ranges or Cordilleras (Figure 1). The Eastern Cordillera of the Colombian Andes that has no equivalent in the Ecuadorian Andes is made of the metamorphic and igneous basement of Precambrian, Paleozoic, and Mesozoic ages, which are covered by thick Paleozoic and Mesozoic sedimentary and volcanoclastic rocks (Sarmiento-Rojas et al., 2006; Mora et al., 2009). The Central Cordillera, which is equivalent to the Cordillera Real in Ecuador, is limited by the Cauca and Magdalena Valleys and is formed in its western flank by a metamorphic belt, formed under amphibolite facies included within the Cajamarca Complex and with Jurassic metamorphic ages, intruded by Cenozoic arc-related granitoids (Blanco-Quintero et al., 2014). This metamorphic belt may have a southern and northern extension and also related in faulted contact with Jurassic plutonic rocks (Bustamante et al., 2017) which are intruding a Permo-Triassic (Villagómez et al., 2011; Bustamante et al., 2016; Leal-Mejía et al., 2019; Spikings et al., 2019) or Proterozoic (Cuadros et al., 2014) basement. Additionally, Cretaceous medium- to high- pressure metamorphic rocks (Bustamante et al., 2011, 2012), volcano-sedimentary sequences, and arc-related granitoids (Jaramillo et al., 2017) are included in the Central Cordillera. Finally, the Western Cordillera is defined as an allochthonous oceanic sequence of volcanic rocks and marine sediments mainly of upper Cretaceous age, related to early interaction between

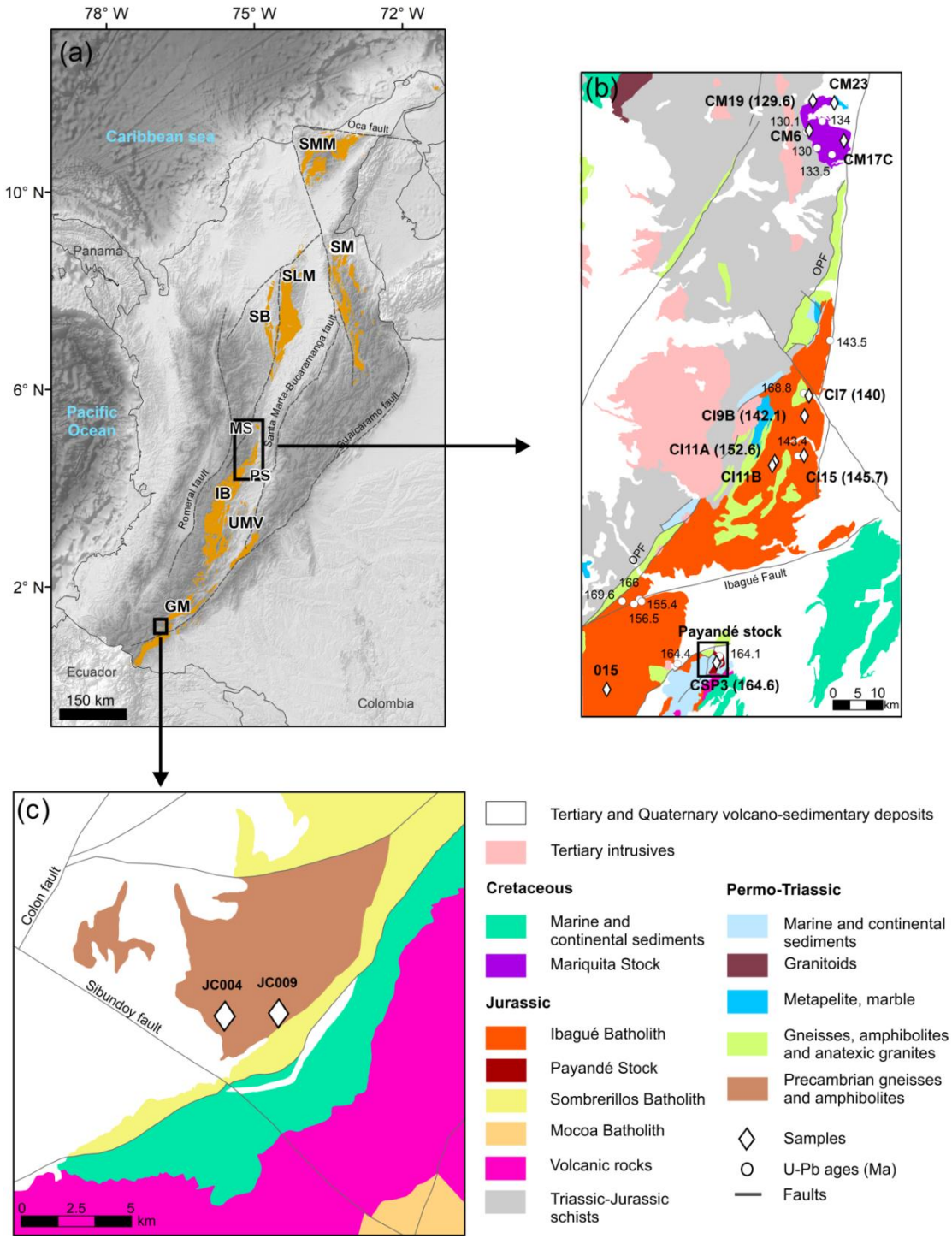

Figure 2. (a) Map showing the location of the studied zones in the Central Cordillera of the Early Jurassic-Early Cretaceous magmatic arc. Insets show the simplified geological maps with the sample locations of the Ibagué Batholith and the Payandé and Mariquita Stocks reported by Bustamante et al., (2016) (b) and Sombrerillos Batholith reported by Restrepo et al., (2020) at the southern part of the arc (c). OPF: Otú-Pericos fault.

the Caribbean plateau with South America (Kerr et al., 1997; Villagómez et al., 2011; Hincapié-Gómez et al., 2018).

The Jurassic to Early Cretaceous magmatic belt in the Northern Andes of Colombia

The Jurassic to Early Cretaceous magmatism in Colombia corresponds to the most long-lived magmatic activity in the Colombian Andes. Its extension includes granitoids from La Guajira, the Santa Marta Massif, the Central Cordillera, the Upper Magdalena Valley, the Garzón Massif and the Eastern Cordillera (Figure 1), forming a discontinuous belt of intrusive and volcanic rocks that intrude a basement composed of Permo-Triassic or older metamorphic rocks formed during the assembly and breakup of Pangea (Aspden et al., 1987; Cochrane et al., 2014; Bustamante et al., 2016; Quandt et al., 2018; Rodríguez et al., 2018; Leal-Mejía et al., 2019). This long-lived magmatism lasted from ca. 200 to 129 Ma and our regional study zone extends in a NE direction from the Mocoa batholith in southern Colombia (Zapata et al., 2016; Rodríguez et al., 2018) to the granitoids from the Sierra Nevada de Santa Marta in the north (Quandt et al., 2018; Figure 1). Its composition is dominantly granodiorite to tonalite with minor diorites to gabbros.

Previous studies have identified some characteristics of the regional configuration and proposed some possible evolutionary scenarios. Cediel et al. (2003), based on the study of sedimentary deposits, proposed that magmatism occurred as a consequence of rifting during the Triassic until the Late Jurassic. Further studies using geochemical parameters such as Nb and Ti negative anomalies, enrichment in light rare earth elements (LREE) compared with heavy REE, are consistent in showing that this magmatism was formed in a continental magmatic arc due to the subduction of the Farallón plate beneath NW South America (Leal-Mejía, 2011; Cochrane et al., 2014; Bustamante et al., 2016; Zapata et al., 2016; Rodríguez et al., 2018; Leal-Mejía et al., 2019). Additionally, Nd, Pb, and Hf isotopic information let Cochrane et al. (2014), Bustamante et al. (2016), Quandt et al. (2018), and Leal-Mejía et al. (2019) to identify a signature progressively more akin with the depleted mantle with time. Thus, based on this new geochemical information and a spatial

Table 1. Distribution of the studied segments in the arc and the geographic zones (ca. 194-130 Ma)

Segment	Latitude (°N)	Zone	Age (Ma)	Unit*
North	~10 to 11	Santa Marta Massif	ca. 186-181	Santa Marta
Central	~6.5 to 9	Segovia Batholith	ca. 167-159	Segovia Batholtih
		San Lucas Massif	ca. 194-182	San Martín de Loba-Juana Sánchez granodiorites Norosí Batholith Papayal Monzonite
South	~1 to 5	Mariquita Stock	ca. 134-130	Mariquita Stock
		Payandé Stock	ca. 164-165	Payandé Stock
		Ibagué Batholith	ca. 189-140	Ibagué Batholith
		Upper Magdalena Valley	ca. 192-173	El Astillero Quartz monzodiorite Páez Quartz monzodiorite Anchique Quartz monzonite San Cayetano Quartz monzonite Los Naranjos Quartz monzonite Las Minas Monzodiorite
		Garzón Massif	ca. 189-152	Algeciras Monzodiorite Altamira Monzodiorite Garzón Granite Sombrerillos Batholith Mocoa Batholith

* Data from each unit in the Supplementary Data Table 1.

distribution pattern, some researches proposed a subduction slab rollback model, where, the Farallon plate and the magmatism migrated progressively toward the west from ca. 193 to 145 Ma (Leal-Mejía, 2011; Cochrane et al., 2014; Spikings et al., 2015, 2019; Quandt et al., 2018; Leal-Mejía et al., 2019). Afterward, Bustamante et al. (2016) observed that in the southern segment of the arc, the areal expression of the plutonic rocks diminished in size until the early Cretaceous, as seen in the northernmost segment of the Ibagué Batholith and the Mariquita Stock (Figure 2). They suggested that this distribution and the detrital zircon age variations may be explained by a progressive decrease in the magmatism produced by an oblique subduction configuration. The oblique subduction scenario is based on paleomagnetic and sedimentary basin studies and suggested that some blocks were formed southernmost of the actual position and migrated along-margin (Bayona et al., 2006, 2010,

2020). This model implication indicates that the igneous blocks may have formed in a different geographic position to the current one and, additionally, the arc is formed by some blocks in situ and some that have migrated.

3. Methods

3.1. Whole-rock geochemistry compilation

We compiled a geochemical database from published papers, master and Ph.D. thesis, as well as reports from the Colombian Geological Survey. The database includes 225 whole-rock geochemistry analyses, including major and trace elements, and the related zircon U-Pb geochronology of the plutonic rocks associated with the Jurassic to Early Cretaceous magmatism in the Central Cordillera of Colombia between ca. 194 to ca. 130 Ma (65 analyses). We only used geochemical data with related geochronological data to estimate crustal characteristics (REE ratios and patterns) and saturation temperatures. Data were filtered with major element totals from 97 to 103 wt% to remove altered samples. Compiled data is available in the Supplementary Data Tables 1 to 3.

Saturation temperatures were estimated based on the whole-rock geochemistry content of the accessory phases of zircon and apatite. For zircon saturation temperatures, we used the updated method of Boehnke et al. (2013) that is based on the concentration of major elements of the rock and the Zr content. In the apatite saturation temperatures, we applied the methods of Harrison and Watson (1984) for metaluminous samples (A/CNK <1) and Bea et al. (1992) for peraluminous rocks (A/CNK >1). The apatite estimation is based on the influence of the P_2O_5 and SiO_2 contents, and the whole-rock composition.

On the other hand, the REE are geochemical tracers that can be used to estimate the magma source depth and the crustal thickness. The REEs in the magmas are affected mainly by the interaction with garnet, amphibole, plagioclase, and pyroxene in the lower crust (Kay et al., 1999; Kay and Mpodozis, 2001; Mamani et al., 2010; Wörner et al., 2018). $(La/Yb)_N$ indicates the pattern steepness, and it is related to garnet and amphibole fractionation in the magma source (Kay et al., 1999; Mamani et al., 2010). Thus, higher ratios suggest higher

magma genesis pressures and, therefore, crustal thickening (Kay et al., 1999, 2005). The field of magma equilibration with amphibole-bearing mineral residues is around 40 to 50 km (Kay et al., 1999; Kay and Mpodozis, 2001). Concerning Eu, the negative Eu anomaly suggests that magma processes such as melting, fractionation, or accumulation occurred shallower than the plagioclase stability limit of 40-45 km (Saleeby et al., 2003; Girardi et al., 2012; Winter, 2014) and the lack of anomaly suggests that the magma genesis occurred deeper than this limit.

3.2. Mineral chemistry

Thirteen samples from the southern arc segment belonging to the Ibagué Batholith, Mariquita, and Payandé stocks in Tolima (reported by Bustamante et al., 2016) and the Sombrerillos Batholith in Putumayo (reported by Restrepo et al., 2020) were studied for mineral chemistry analyses of plagioclase, biotite, pyroxene, and amphibole. The ages were assigned according to U-Pb geochronological data analyzed in the samples and reported by Bustamante et al. (2016) and Restrepo et al. (2020) or by association with spatially close samples (Figure 2). We used a JEOL JXA-8230 electron microprobe from the Department of Petrology and Metalogenesis at the Instituto de Geociências e Ciências Exatas of UNESP University at Rio Claro, Brazil. Analyses were performed with a beam current of 20 nA and an accelerating voltage of 15 kV. Counting time was 10 s and 20 s for major and minor elements, respectively. The standards used for element calibrations were wollastonite (Ca), orthoclase (Si and K), albite (Na), diopside (Mg), anorthite (Al), ilmenite (Ti and Fe), chromite (Cr), rhodonite (Mn), synthetic NiO (Ni), apatite (F), sodalite (Cl) and barite (Ba). Results are presented in the Supplementary Data Table 4.

Pressure and emplacement depth were constrained using the amphibole and plagioclase chemistry analyses in the Ibagué Batholith (CI11B, CI15, CI7), the Mariquita Stock (CM17C, CM6), and Sombrerillos Batholith (JC004) (Figure 14). We estimated pressure and temperature of magma crystallization based on the iteration of the Anderson and Smith, (1995; calibration error= ± 0.6 kbars) amphibole barometer with the hornblende-plagioclase thermometer of Holland and Blundy, (1994; calibration error= ± 40°C) (reaction edenite +

albite = richterite + anorthite) using the Anderson et al., (2008) calculation spreadsheet. Estimations were calculated wherever possible in amphibole rims, but cores were also selected when the rims would have high Si content. We preserved all the data points in the homogeneous amphiboles, the core points in the Si-poor core Si-rich rim amphiboles, and the rim points in the Si-rich core Si-poor rim amphiboles. Plagioclase compositions were not measured in contact with amphibole, so we applied average plagioclase rim composition for each sample to the thermometer and compared barometric results with the calibrations of Schmidt, (1992; calibration error= ± 0.6 kbars) and Mutch et al., (2016; calibration error= ± 0.5 kbars). Nevertheless, temperatures and pressures of Holland and Blundy (1994) and Anderson and Smith (1995), respectively, are acceptable approximations taking into account that other thermobarometric calibrations like the one from Ridolfi and Renzulli (2012) are unsuitable for our samples on account of the required compositional ranges to obtain accurate results.

3.3. Whole-rock Sr isotopes

New whole-rock Sr isotope analysis of the Ibagué Batholith (3 samples) presented in this work was acquired using a Thermo-Finnigan Neptune multi-collector system at Washington State University, and the results are shown in the Supplementary Data Table 5. The analyzed samples correspond to a pyroxene-bearing quartz diorite (CI9B), a clinopyroxene-bearing granodiorite (CI11A), and a granodiorite (CI7). The procedures for the preparation and dissolution of the samples for the isotopes of Sr are the same as those reported by Gaschnig et al. (2011). Sr analyzes were corrected for mass fractionation with $^{86}Sr/^{88}Sr$ = 0.1194 and normalized with NBS-987. The $^{87}Sr/^{86}Sr$ average reproducibility with 2σ was ± 0.00005. The initial isotopic values were calculated using the Rb and Sr concentrations of analyzes made by X-ray fluorescence in the same samples and reported in Bustamante et al. (2016).

4. Results

In the following section, we show the results obtained for the Jurassic arc in the Central Cordillera in Colombia from 194 to 130 Ma. In a regional approach, we integrate the whole-rock geochemical and geochronological data in order to estimate the saturation temperatures and evaluate the magma source depth and crustal thickness through the variations of the REE patterns and ratios. In a local approach, we analyze the emplacement conditions of a segment of the southern part of the arc through mineral chemistry analyses and thermobarometry.

4.1. Zircon and apatite saturation temperature

Figure 3 shows that Zr (ppm) and P_2O_5 (wt%) have a negative correlation with SiO_2 (wt%). In a SiO_2 range from 62 to 77 wt%, the Zr content varies from 69 to 299 ppm. To reduce the zircon inheritance –which would increase the Zr concentration and thus the zircon saturation temperature (Siégel et al., 2018)- we used samples with SiO_2 >64 wt%, which have a Zr concentration from 87-299 ppm. P_2O_5 (wt %) ranges from 0.05 to 0.65 with the maximum concentrations in the granitoids from the Upper Magdalena Valley (0.13-0.65, average 0.27 ±0.17 wt%).

Zircon saturation temperatures are <800 °C ranging from 674 to 778 °C (average 725 ±26 °C) and apatite ones range from 796 to 943 °C (average 887 ±33 °C). For samples older than 165 Ma, saturation temperatures are variable, but they are usually higher (676-778 °C for zircon and 817-969 °C for apatite temperatures) compared with the lower temperatures after 165 Ma (674-757 °C for zircon 796-933 °C for apatite temperatures). Granitoids from Garzón Massif (Figure 1) display the highest zircon and apatite saturation temperatures at 172 Ma.

After 165 Ma, the Payandé Stock and Ibagué Batholith display the lowest saturation temperatures. The former shows a minimum zircon saturation temperature of 674 °C at 164 Ma, and the latter has the lowest apatite saturation temperature of 796 °C at 155 Ma (Figure 3). An increasing trend is observed from the end of the Middle Jurassic until the Early Cretaceous in the zones belonging to the central segment of the arc (Segovia Batholith, Ibagué Batholith, and Mariquita Stock) where the Mariquita Stock displayed the highest

temperatures from 133-130 Ma yielding zircon and apatite saturation of 724-757 °C and 885-933 °C, respectively.

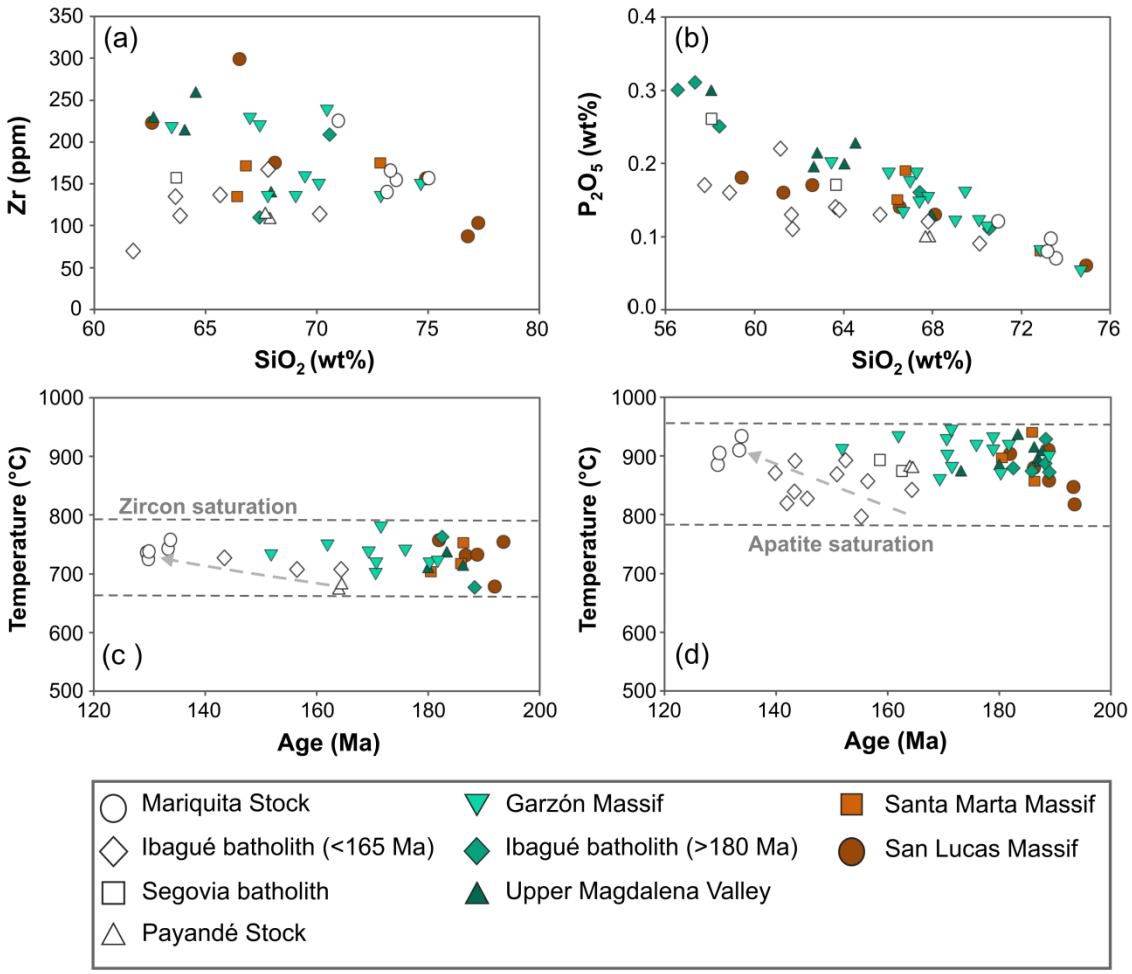

Figure 3. (a) Zr (ppm) vs. SiO_2 (wt%). (b) P_2O_5 (wt%) vs. SiO_2 (wt%). Relation of age with zircon (c) and apatite (d) saturation temperatures. The gray dashed lines are enclosing the range of each temperature.

4.2. Crustal thickness evaluation

Chondrite-normalized (McDonough and Sun, 1995) REE patterns are shown in Figure 4. Patterns are divided into eight zones according to the geologic and geographic characteristics and ages. The whole data from all the zones are shown in the gray field and is overlapped by the individual data displayed in black lines. To constrain the geochemical

variations trough time accurately, the Ibagué Batholith was subdivided into southern and older (189-183 Ma) and northern and younger (164-151 Ma) samples.

In general, for the analyzed samples (SiO_2= ~50-77 wt%) the Early Jurassic to Early Cretaceous REE behavior is characterized by moderate to steep slopes [$(La/Yb)_N$=4.1-20.1], light REE (LREE) enrichment [$(La/Sm)_N$=2.6-8] and nearly flat heavy REE (HREE) depletion [$(Dy/Yb)_N$=0.5-1.3, $(Sm/Yb)_N$= 1.0-3.7]. Eu anomalies (Eu/Eu*) are variable from pronouncedly negative to moderately positive (Eu/Eu*=0.2-1.5) with more than 65% of the studied samples with negative anomaly and some of them (Segovia and Ibagué batholiths), mainly during the Middle to Late Jurassic lacking the anomaly (Eu/Eu* ~1) or with a slight development.

The behavior of the differentiation (SiO_2) with the REE slope [$(La/Yb)_N$], the HREE [$(Dy/Yb)_N$] and the Eu anomaly (Eu/Eu*) are shown in Figure 5, as well as the variation of the LREE [$(La/Sm)_N$] with the HREE [$(Sm/Yb)_N$]. La/Yb correlates positively with silica, and heavy REE decreases slightly as the differentiation increase, showing a negative correlation between $(Dy/Yb)_N$ and silica in Figure 5b. The ratio is overall similar in the studied samples, and they vary in a restricted range. Light and heavy REE expressed as $(La/Sm)_N$ and $(Sm/Yb)_N$ are uncorrelated (Figure 5c). Furthermore, Eu/Eu* decrease with high silica reaching the lowest values (0.2-0.7) from a SiO_2>73 wt%.

The samples from the granitoids of San Lucas Massif (194-182 Ma) could be divided into two groups, one similar to the youngest zone of Mariquita Stock (134-130 Ma) with a relatively flat slope [$(La/Yb)_N$= 4.8-6.4] and depleted LREE and HREE patterns, low normalized Sm/Yb (1-2.3) and La/Sm (2.7-5.0) ratios and a strong negative anomaly. Another group displays a gull-shaped pattern, LREE enrichment, and an extreme negative anomaly (0.2-0.4) that could be an effect of the high differentiation (SiO_2 >76 wt%).

The granitoids from the other zones (Santa Marta Massif, Upper Magdalena Valley, Garzón Massif, Ibagué Batholith, and Segovia Batholith) formed between 192 to 143 Ma are

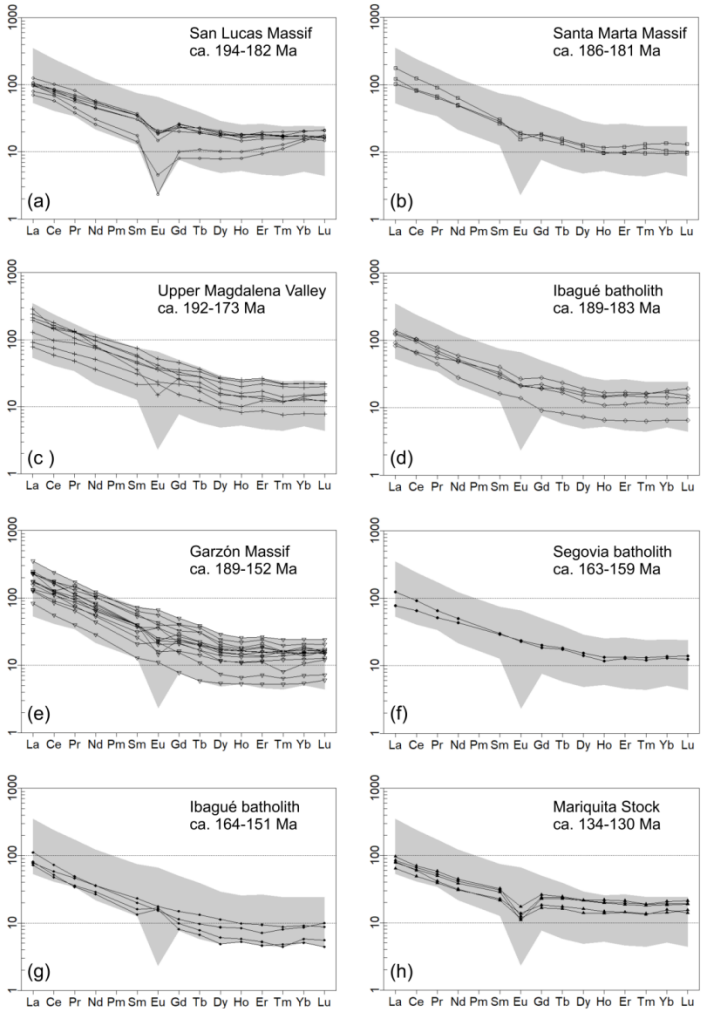

Figure 4. REE patterns normalized to Chondrite from McDonough and Sun (1995) for intrusive rocks from: (a) San Lucas Massif (ca. 194-182 Ma); (b) Santa Marta Massif (ca. 189-181 Ma); (c) Upper Magdalena Valley (ca. 192-173 Ma); (d) Ibagué Batholith (ca. 189-183 Ma); (e) Garzón Massif (ca. 189-152 Ma); (f) Segovia batholith (ca. 163-159 Ma); (g) Ibagué Batholith (ca. 164-151 Ma); (h) Mariquita Stock (ca. 134-130 Ma). Gray field background in each plot represents all the sample patterns. Data from Supplementary Data Table 2.

characterized by steeper REE patterns and higher $(La/Yb)_N$ ratios compared with the San Lucas Massif and Mariquita Stock. The $(La/Yb)_N$ values decrease moderately between 192 to 150 Ma, ranging from the maximum 20.2 at ca. 192 Ma in the granitoids from the Upper Magdalena Valley to 15.3 at ca. 152 Ma in the Garzón Massif. Additionally, during this period, they are more enriched in LREE and HREE, displaying higher $(Sm/Yb)_N$ and

$(La/Sm)_N$ from 1.7-3.7 and 2.6-8.0, respectively. The granitoids from the Upper Magdalena Valley (192-173 Ma) and Garzón Massif (189-152 Ma) located in the southern part of the arc show the widest diversity in patterns with the former displaying the most enriched HREE [$(Sm/Yb)_N$=2.1-3.7]. In the north, the granitoids from Santa Marta Massif (189-181 Ma) have normalized La/Yb ranging from 9.7 to 13.1 and Sm/Yb from 2.2 to 2.8. The southern and oldest zone of the Ibagué Batholith (189-183 Ma) behaves similar to the northern and youngest zone (164-151 Ma), but in comparison, the north has mostly steeper patterns [$(La/Yb)_N$=8.5-15.8], LREE is more enriched [$(La/Sm)_N$=3.3-6.0] and has mostly slightly developed to positive Eu anomalies (Eu/Eu*= 0.9-1.5).

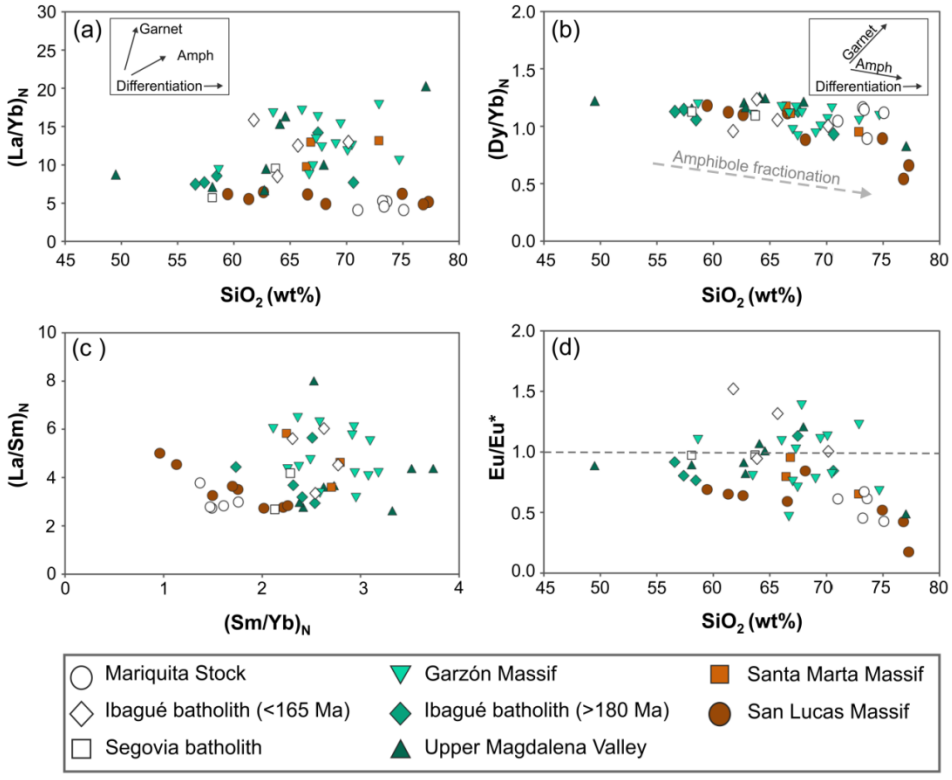

Figure 5. REE ratios variation. (a) (La/Yb)N vs. SiO2 (wt%). (b) (Dy/Yb)N vs. SiO2 (wt%). (c) (La/Sm)N vs. (Sm/Yb)N. (d) Eu/Eu* vs. SiO2 (wt%). N denotes normalized ratios to Chondrite of McDonough and Sun (1995). Plots inset in (a) and (b) shows expected fractionation for amphibole and garnet with differentiation. The dashed gray line in (d) separates positive (>1.0) to negative (<1.0) anomaly. Amph, Amphibole.

As shown above, REE ratios are a tracer of the geochemical variability throughout the Early Jurassic to the Early Cretaceous (194-130 Ma). They can also be used as indicators to estimate the crustal thickness variations quantitatively or to indicate thickening and thinning episodes. Commonly Sr/Y and La/Yb ratios have been used because they track the presence of plagioclase (Sr and La) and garnet-amphibole (Y and Yb) in the fractionation during the magmatic assimilation in the crust (Chapman et al., 2015; Chiaradia, 2015; Profeta et al., 2015). We used the method of Profeta et al. (2015) and compared the $(La/Yb)_N$ with the Sr/Y ratios as proxies to determine crustal variation trends.

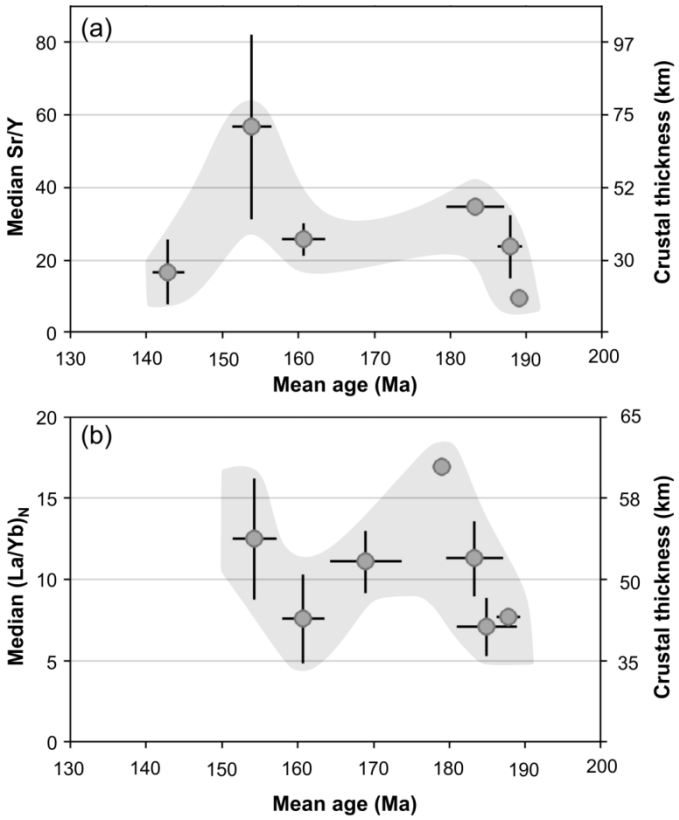

Figure 6. (a) Median Sr/Y vs. Mean age (Ma) for the Jurassic arc for the period between 190 to 140 Ma calculated following the method of Profeta et al. (2015). (b) Median (La/Yb)N vs. Mean age (Ma) for the Jurassic arc from 190 to 150 Ma The left vertical axis is scaled for Sr/Y (a) and (La/Yb)N (b), and the right axis shows the equivalent crustal thickness. Gray field in the background is showing the crustal thickness interpreted trend in the data. Bars in each point mean 1σ error. N means normalized to chondrite from McDonough and Sun (1995).

We selected samples with geochronological data related and applied several filters following Profeta et al. (2015) method to choose rocks with intermediate compositions, for example, SiO_2 from 55-68 wt%, MgO <4 wt%, and mean Rb/Sr from 0.05-0.2. After data filtration, seventeen samples from 189 to 143 Ma were used for Sr/Y calculations belonging to Santa Marta Massif, Ibagué and Segovia batholiths and, Garzón Massif. For La/Yb, nineteen samples from 188 to 154 Ma passed the filters, and besides Upper Magdalena Valley, zones are the same as for Sr/Y estimations.

Median Sr/Y and $(La/Yb)_N$ ranges from 9 to 57 and 7 to 17, respectively (Figure 6). It is equivalent to a crustal thickness of 20 to 70 km for the Sr/Y range and 40 to 60 km for La/Yb, according to Profeta et al. (2015) estimations. Therefore, these results show that crustal thickness values between Sr/Y and La/Yb do not agree inside the period from 190 to 140 Ma, but Figure 6 indicates that both ratios are showing similar crustal variation episodes meaning that the geochemical proxies are in phase. The trends displayed that during the periods 190-180 Ma (Santa Marta Massif, Upper Magdalena Valley, and Ibagué Batholith) and 160-154 Ma (Ibagué Batholith), the crustal thickness increases, reaching the highest value at 154 Ma. In contrast, during the periods 180-160 Ma (Garzón Massif and Segovia Batholith) and 154-143 Ma (Ibagué Batholith), the crust is thinner.

4.3. Petrography and mineral chemistry

Thirteen samples from the southern arc segment belonging to the Ibagué Batholith (ca. 152-140 Ma), Mariquita (134-130 Ma), and Payandé (ca. 165 Ma) stocks in Tolima, and Sombrerillos Batholith (ca. 152 Ma) in Putumayo were analyzed. They vary from diorites to granites. Samples are mainly inequigranular, hypidiomorphic, and medium-grained composed of quartz sometimes with undulose extinction, plagioclase mostly zoned (Figure 7a), and minor K-feldspar with occasional myrmekite and tartan textures (Figure 7b).

Mafic minerals include amphibole as the most abundant constituent, which is commonly twinned and occasionally skeletal (Figure 7c). Tonalite CM23 from the Mariquita Stock is the only one without amphibole. Biotite sometimes shows symplectic intergrowths of quartz in the Sombrerillos Batholith (JC004) and is bent or defining a lineation in sample

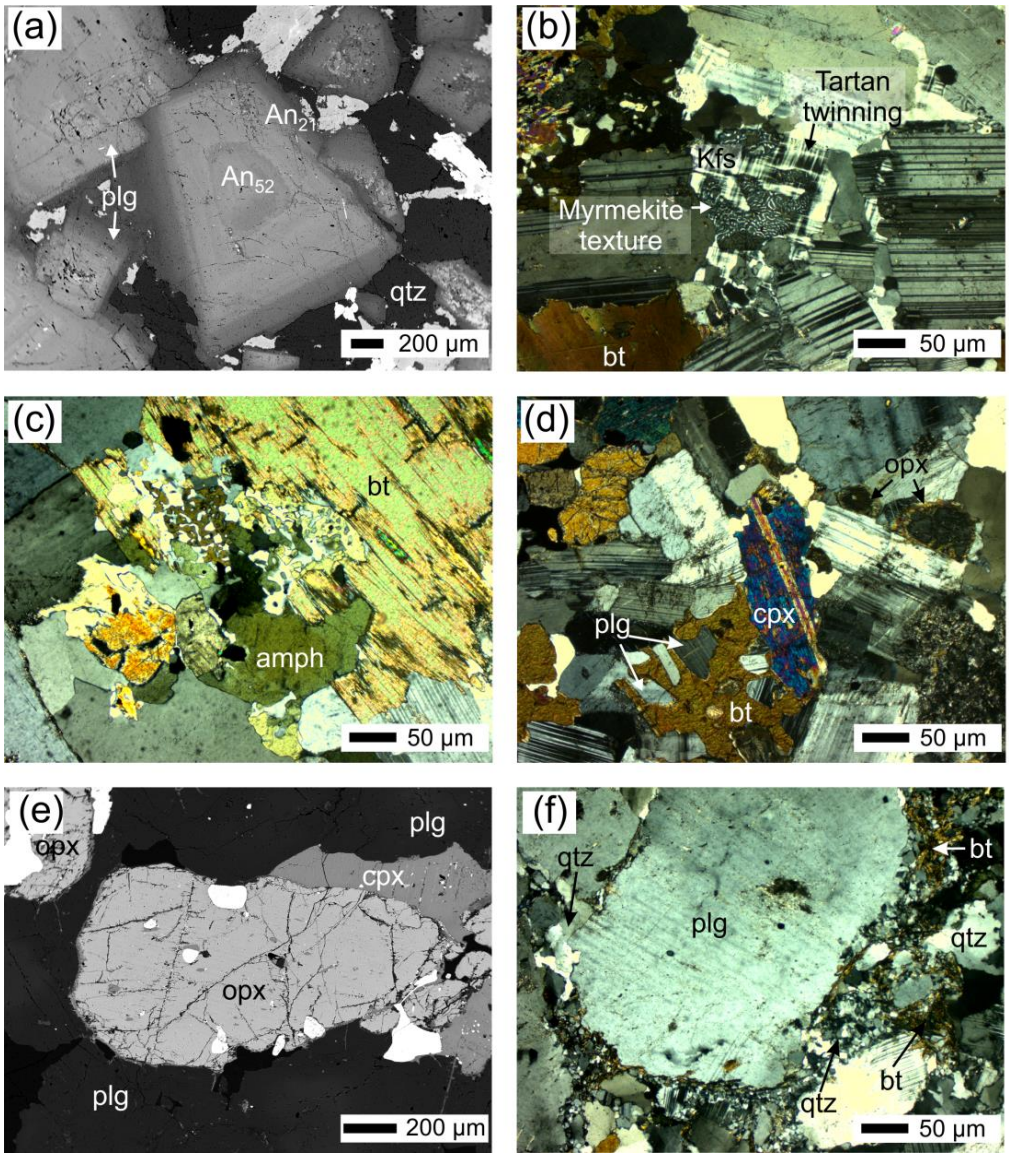

Figure 7. Photomicrographs of samples from the Payandé Stock and Ibagué and Sombrerillos Batholiths. (a) Back-scattered electron (BSE) image of zoned plagioclase of a granodiorite (sample CSP3) from the Payandé Stock. This plagioclase has an anorthite (An) rich-core with labradorite composition and a more sodic rim with oligoclase composition. (b) Diorite (sample JC009) from the Sombrerillos Batholith with tartan twinning and myrmekite intergrowth in K-feldspar. (c) Clinopyroxene-bearing diorite (sample CI15) from the Ibagué Batholith with amphibole type magnesiohornblende showing a skeletal texture in contact with biotite. (d) Pyroxene-bearing quartz diorite (sample CI9B) from the Ibagué Batholith showing biotite oikocryst containing resorbed plagioclases in contact with twinned clinopyroxene type diopside and (e) BSE image showing orthopyroxene type enstatite in contact of diopside and plagioclase. (f) Granodiorite (sample CI7) from the Ibagué Batholith showing deformed textures in quartz, plagioclase, and biotite (annite type). (b) to (d) and (f) are microscope cross-polarized light images. amph, amphibole; bt, biotite; cpx; clinopyroxene; Kfs, K-feldspar; opx, orthopyroxene; plg, plagioclase; qtz, quartz.

CI11A and CI11B or has a poikilitic texture hosting some plagioclase crystals as in sample CI9B from the Ibagué Batholith (Figure 7d). It also shows a cumulate texture in the Payandé Stock. Pyroxene is a mineral restricted to some samples of the Ibagué Batholith. Diopside and enstatite (Figure 7e) appear as inclusions in plagioclase in sample CI9B.

Zircon, apatite, and Fe-Ti oxides are typical accessory phases, and titanite appears in some samples of the Ibagué Batholith (CI11A and CI11B), Mariquita Stock (CM23) and Sombrerillos Batholith. Samples show low to medium alteration level, and typically, plagioclase is replaced by sericite or epidote, and biotite is altered into chlorite.

The northernmost and youngest rock of the Ibagué Batholith is a granodiorite (CI7) that shows zoned plagioclases and deformation textures such as oriented amphiboles and biotites, and quartz displaying subgrain rotation and grain boundary migration textures (Figure 7f).

4.3.1. Plagioclase composition

Plagioclase composition in the studied plutons is mainly represented by andesine and minor albite (Ab) and labradorite with Ab contents from 93 to 43%, Anorthite (An) from 56 to 6%, and Orthoclase (Or) contents below 4% (Figure 8 and Table 2). It shows mainly normal or oscillatory zoning patterns, but in the Sombrerillos Batholith, inverse zoning is common. Anorthite contents in plagioclase cores are from An55 to An18, with most units having grains with An 50 to 30 cores.

In the Payandé Stock, plagioclases have well-developed concentric zoning with An ranging from 52 to 20. Plagioclases have cores with andesine to labradorite (An52-46) compositions and oligoclase rims (An 25-20). Plagioclases range from An56 to An14 in the Ibagué Batholith. There, most plagioclases have An content cores between 55 to 32 with outliers until An18 and rims with a broad An range (An49-14). Concentric and patchy zoning patterns are common, and occasionally discontinuous zoning is shown (pyroxene-bearing quartz diorite CI9B).

Mariquita Stock shows plagioclases that are mainly normally zoned with well-developed concentric zoning and wide An ranges (An47 to An6). An in cores varies typically between 47 to 31, but outliers until 18 are shown and, plagioclase rims have a more extensive range (An 6-35). Sombrerillos Batholith displays plagioclases that are slightly zoned and range from An50 to 25. Cores have high An contents (An50), and rims range from An47 to 28.

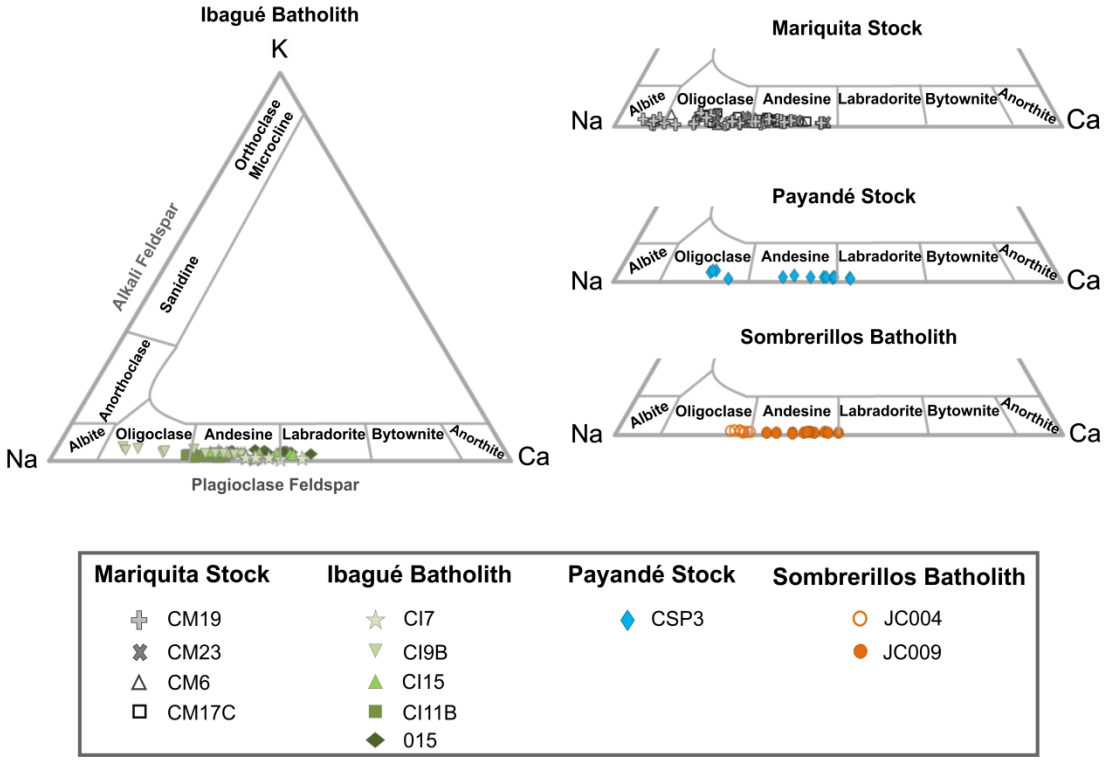

Figure 8. Plagioclase classification of samples from the Mariquita Stock, Ibagué Batholith, Payandé Stock, and Sombrerillos Batholith.

Table 2. Representative plagioclase compositions from the Payandé and Mariquita Stocks and Ibagué and Sombrerillos Batholiths

	Payandé Stock		**Ibagué Batholith**					**Mariquita Stock**		**Sombrerillos Batholith**		
Rock type	Granodiorite		Clinopyroxene-bearing diorite	Pyroxene-bearing quartz diorite		Granodiorite		Tonalite	Granite	Granodiorite		Diorite
Sample	CSP3		CI11B	CI9B		CI7		CM23	CM19	JC004		JC009
Analysis	1-1 core	1-4 rim	3-1 core	1-1 core	1-4 rim	4-1 core	4-3 rim	3-1 core	1-1 rim	4-1 core	4-2 rim	4-1 core
(wt%)												
SiO_2	55.35	63.28	59.25	57.11	63.28	54.13	57.18	57.15	66.33	61.63	60.50	57.09
Al_2O_3	28.32	23.11	25.40	25.97	21.82	29.06	27.36	26.71	21.12	23.94	24.73	26.93
FeO*	0.29	0.19	0.11	0.17	0.21	0.10	0.11	0.01	0.08	0.11	0.35	0.07
CaO	10.80	4.34	7.72	7.83	2.91	11.17	9.18	8.26	1.79	5.22	6.02	8.60
Na_2O	5.32	8.46	7.35	6.80	9.22	5.06	6.26	6.63	10.37	8.45	7.96	6.37
K_2O	0.19	0.53	0.15	0.29	0.61	0.12	0.16	0.24	0.10	0.17	0.12	0.12
Total	100.27	99.92	99.99	98.17	98.05	99.64	100.25	98.99	99.80	99.52	99.68	99.19
Formula calculated for 8 O												
Si	2.490	2.800	2.648	2.604	2.848	2.451	2.558	2.584	2.914	2.746	2.700	2.576
Al	1.501	1.205	1.338	1.396	1.157	1.551	1.443	1.423	1.094	1.257	1.301	1.432
Fe^{2+}	0.011	0.007	0.004	0.006	0.008	0.004	0.004	0.000	0.003	0.004	0.013	0.002
Ca	0.520	0.206	0.370	0.383	0.140	0.542	0.440	0.400	0.084	0.249	0.288	0.416
Na	0.464	0.726	0.637	0.601	0.804	0.444	0.543	0.581	0.883	0.730	0.688	0.557
K	0.011	0.030	0.009	0.017	0.035	0.007	0.009	0.014	0.005	0.010	0.007	0.007
(mol %)												
An	52	21	36	38	14	55	44	40	9	25	29	42
Ab	47	75	63	60	82	45	55	58	91	74	70	57
Or	1	3	1	2	4	1	1	1	1	1	1	1

Note: * Total Fe is given as FeO

4.3.2. Biotite composition and water content

In the Payandé Stock and southern Ibagué Batholith biotite classifies as phlogopite and in northern Ibagué Batholith, Mariquita Stock, and Sombrerillos Batholith as annite. (Figure 9 and Table 3) according to Mg/(Mg+Fe) and Al(total) values. The Mg-numbers (Mg#) ranges from 0.35 to 0.59 apfu with the highest values in the diorite 015 (0.58-0.59) in the Ibagué Batholith and the lowest in the granite CM19 (0.35-0.37) in the Mariquita Stock.

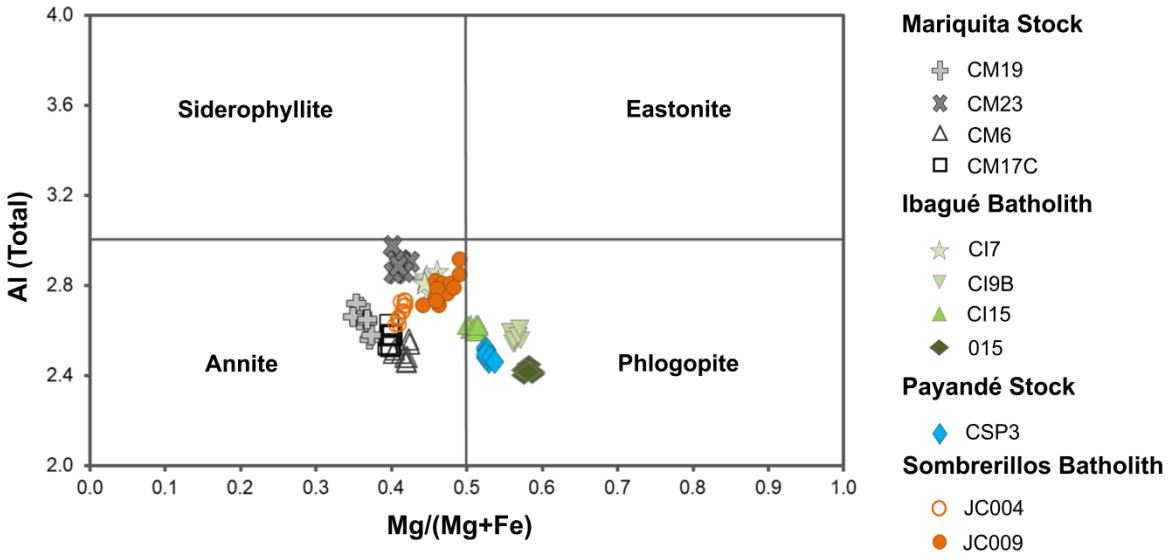

Figure 9. Biotite classification of samples from the Mariquita Stock, Ibagué Batholith, Payandé Stock and Sombrerillos Batholith.

The Al_{tot} ranges from 2.40 to 2.97 apfu, and the Mariquita Stock is more Al-rich than the other units. Biotites display a broad Ti content from 0.22 to 0.60 apfu with the pyroxene-bearing quartz diorite CI9B displaying the highest value (0.51-0.6), and the diorite JC009 showing the lowest (0.22-0.41). H_2O content varies between 3.72 to 3.90 wt%, and it was calculated following Tindle and Webb (1990). Cl contents in biotites have a wide range

Table 3. Representative biotite compositions from the Payandé Stock, Ibagué batholith, Mariquita Stock and Sombrerillos Batholith

	Payandé Stock	Ibagué batholith				Mariquita Stock				Sombrerillos Batholith	
Rock type	Granodiorite	Diorite	Clinopyroxene-bearing diorite	Pyroxene-bearing quartz diorite	Granodiorite	Granite			Tonalite	Granodiorite	Diorite
Sample	CSP3	15	CI5	CI9B	CI7	CM17C	CM6	CM19	CM23	JC004	JC009
Analysis	3-3	3-1	3-1	2-2	1-2	2-3	2-2	2-3	1-3	3-1	3-1
(wt%)											
SiO_2	36.15	37.00	35.15	36.32	35.37	35.61	35.48	35.52	34.94	35.49	35.48
TiO_2	3.85	3.74	3.53	5.22	3.32	4.12	3.75	3.79	3.74	3.33	1.86
Al_2O_3	13.40	13.20	14.21	14.37	15.37	14.10	13.73	14.23	16.02	14.84	15.30
FeO	18.49	16.45	19.29	16.74	21.01	22.13	22.13	23.85	21.13	22.20	19.50
MnO	0.30	0.27	0.20	0.11	0.31	0.32	0.33	0.41	0.49	0.36	0.35
MgO	12.03	13.18	11.55	11.87	9.51	8.18	9.15	7.21	7.95	8.94	10.55
CaO	0.00	0.00	0.00	0.00	0.00	0.00	0.00	0.00	0.00	0.00	0.00
Na_2O	0.09	0.11	0.08	0.08	0.12	0.05	0.07	0.05	0.04	0.07	0.06
K_2O	9.08	9.09	9.28	9.23	9.02	9.10	8.92	9.09	9.10	9.34	9.32
BaO	0.49	0.31	0.16	0.33	0.47	0.33	0.42	0.23	0.24	0.40	0.16
Cl	0.25	0.08	0.28	0.24	0.05	0.01	0.01	0.02	0.01	0.13	0.21
Total	94.12	93.43	93.72	94.51	94.55	93.96	93.99	94.40	93.65	95.11	92.77
Formula calculated for 22 O											
Si	5.620	5.708	5.511	5.556	5.518	5.624	5.606	5.626	5.500	5.553	5.607
Al^{iv}	2.380	2.292	2.489	2.444	2.482	2.376	2.394	2.374	2.500	2.447	2.393
Al^{vi}	0.076	0.107	0.136	0.146	0.344	0.248	0.162	0.284	0.472	0.289	0.458
Ti	0.450	0.433	0.416	0.601	0.390	0.490	0.446	0.452	0.443	0.391	0.221
Fe	2.404	2.123	2.530	2.141	2.741	2.922	2.924	3.160	2.782	2.905	2.577
Mn	0.039	0.036	0.026	0.014	0.041	0.043	0.044	0.055	0.065	0.048	0.047
Mg	2.787	3.030	2.700	2.707	2.211	1.926	2.154	1.703	1.866	2.086	2.485
Ca	0.000	0.000	0.000	0.000	0.000	0.000	0.000	0.000	0.000	0.000	0.000
Na	0.026	0.033	0.023	0.024	0.037	0.015	0.020	0.014	0.011	0.021	0.018
K	1.801	1.788	1.856	1.801	1.795	1.834	1.798	1.837	1.827	1.864	1.878
Ba	0.030	0.019	0.010	0.020	0.029	0.021	0.026	0.014	0.015	0.025	0.010
OH*	3.934	3.979	3.926	3.938	3.987	3.998	3.996	3.996	3.998	3.965	3.944
Cl	0.066	0.021	0.074	0.062	0.013	0.002	0.004	0.004	0.002	0.035	0.056
Al total	2.46	2.40	2.63	2.59	2.83	2.62	2.56	2.66	2.97	2.74	2.85
Fe/(Fe+Mg)	0.46	0.41	0.48	0.44	0.55	0.60	0.58	0.650	0.599	0.582	0.509
Mg/(Mg+Fe)	0.54	0.59	0.52	0.56	0.45	0.40	0.42	0.35	0.40	0.42	0.49
H2O* (wt%)	3.79	3.87	3.75	3.86	3.83	3.79	3.79	3.78	3.81	3.80	3.74

Note: *H_2O (wt%) was calculated using the Tindle and Webb (1990) method

from 0.001 to 0.074 apfu with the highest values (>0.050 apfu) in the Ibagué Batholith (Diorite CI15 and Pyroxene-bearing quartz diorite CI9B), Payandé Stock (granodiorite CSP3) and in the Sombrerillos Batholith (diorite JC009) and the lowest Cl contents (below 0.006 apfu) in the Mariquita Stock.

4.3.3. Pyroxene composition

Representative pyroxene compositions from Ibagué Batholith Pyroxene-bearing quartz-diorite (CI9B) are given in Table 4 and plotted in Figure 10. Cation proportions were calculated based on six oxygens and plotted using the spreadsheet ternary plot of Marshall, (1996). The studied pyroxenes are clino- and orthopyroxenes, and compositions can be variable in the same sample. The clinopyroxene is mainly diopside with minor augite, composition Wo36-47 En37-41 Fs15-23 and the Mg# is 66.4-73.5. Orthopyroxene is mostly enstatite and pigeonite subordinate with Wo1-8 En53-60 Fs38-42 composition and Mg# = 58.1-61.7.

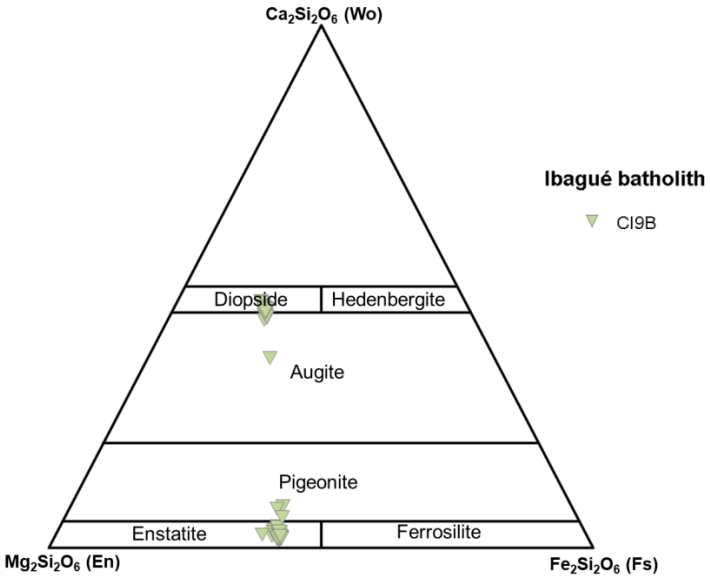

Figure 10. Pyroxene classification of sample pyroxene-bearing quartz diorite CI9B from the Ibagué Batholith.

Table 4. Representative pyroxene compositions from Ibagué batholith

	Ibagué batholith						
Rock type	Pyroxene-bearing quartz diorite						
Sample	CI9B						
	Orthopyroxenes				Clinopyroxenes		
Analysis	1-9	2-4	3-1	4-6	1-10	2-2	3-7
(wt%)							
SiO_2	51.36	50.76	51.70	51.29	51.72	51.67	51.47
TiO_2	0.17	0.12	0.08	0.11	0.14	0.30	0.29
Al_2O_3	0.76	0.78	0.66	1.35	1.15	1.52	1.48
Cr_2O_3	0.01	0.03	0.01	0.00	0.00	0.00	0.01
FeO	23.94	23.23	24.50	21.72	9.07	10.50	9.81
MnO	0.72	0.67	0.81	0.57	0.33	0.38	0.33
MgO	19.87	18.18	19.78	19.64	12.83	13.22	12.97
CaO	1.55	3.72	0.72	1.08	22.38	20.65	22.04
Na_2O	0.03	0.06	0.02	0.04	0.32	0.33	0.39
Total	98.41	97.54	98.27	95.81	97.94	98.58	98.78
Formula calculated for 6 O							
Si	1.969	1.972	1.988	2.008	1.974	1.964	1.949
Al^{iv}	0.031	0.028	0.012	0.000	0.026	0.036	0.051
Al^{vi}	0.003	0.007	0.018	0.070	0.026	0.032	0.015
Fe^{2+}	0.747	0.737	0.788	0.711	0.274	0.322	0.264
Fe^{3+}	0.020	0.018	0.000	0.000	0.016	0.012	0.047
Cr	0.000	0.001	0.000	0.000	0.000	0.000	0.000
Ti	0.005	0.004	0.002	0.003	0.004	0.009	0.008
Mn	0.023	0.022	0.026	0.019	0.011	0.012	0.011
Mg	1.135	1.053	1.134	1.147	0.730	0.749	0.732
Ca	0.064	0.155	0.030	0.045	0.915	0.841	0.894
Na	0.002	0.004	0.001	0.003	0.024	0.024	0.028
(mol %)							
Wo	3	8	1	2	47	43	46
En	57	53	57	60	38	39	38
Fs	40	39	41	38	15	18	17
Mg/(Mg+Fe)	60.3	58.8	59.0	61.7	72.7	69.9	73.5

4.3.4. Amphibole composition

The studied amphiboles belong to the calcic amphibole group, and compositions are variable in the same sample. Representative analyses with cation proportions based on 22

oxygens (Leake et al., 1997) are given in Table 5 and plotted in Figure 11. They classify mainly as magnesiohornblende; however, some samples have other minor compositions. Mariquita Stock and Payandé Stock have minor actinolite; the Sombrerillos Batholith has ferro-hornblende subordinate, and the granodiorite CI7 in the Ibagué Batholith has minor ferro-tschermakite and tschermakite compositions. The Mg# [Mg/(Mg+Fetot)] varies between 0.40 to 0.69 wt%. It decreases along time, showing the highest Mg# in Payandé Stock (0.62-0.69 wt%; 164.6 Ma) and the lowest in the granodiorite CI7 (0.40-0.47 wt%; 140 Ma) in the Ibagué Batholith. However, Mariquita Stock does not follow this trend.

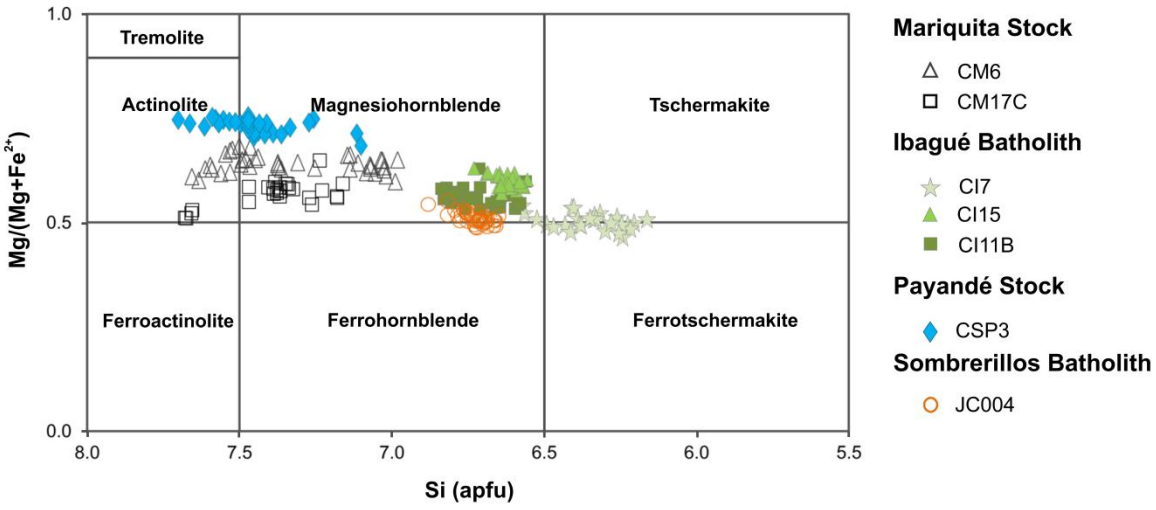

Figure 11. Amphibole classification of samples from the Mariquita Stock, Ibagué Batholith, Payandé Stock and Sombrerillos Batholith. Classification after Leake et al. (1997).

The total Al content in the amphiboles has a wide variation ranging from 0.40 to 2.37 apfu. Two groups are observed based on the Al_{tot} content of the amphiboles in the plutons studied (Figure 12). The high Altot group (>1.34 apfu) is formed by the Ibagué Batholith (CI11B, CI15, and CI7) and the Sombrerillos Batholith (JC004). It has a Mg# between 0.40-0.54, high $(Na+K)_A$ values from 0.23 to 0.50 apfu and high Ti content (0.074-0.248 apfu). In this group Cl (wt%) content could be subdivided into two subgroups: high Cl (>0.10) that includes the CI11B and CI15 and the low Cl (<0.10), which gathers the CI7 and the JC004. The low Altot group (<1.34 apfu) includes the Mariquita (CM6 and CM17C) and the

Payandé stocks (CSP3). It has a variable Mg# that could be subdivided into two groups with similar trends. The first has low Mg# (0.47-0.55), which includes the Mariquita Stock (CM17C and CM6), and the second is high Mg# (>0.6) that includes the Payandé Stock. The low Altot group has a low $(Na+K)_A$ (<0.15 apfu), low Ti (0.003-0.129 apfu), and low Cl (<0.10 wt%).

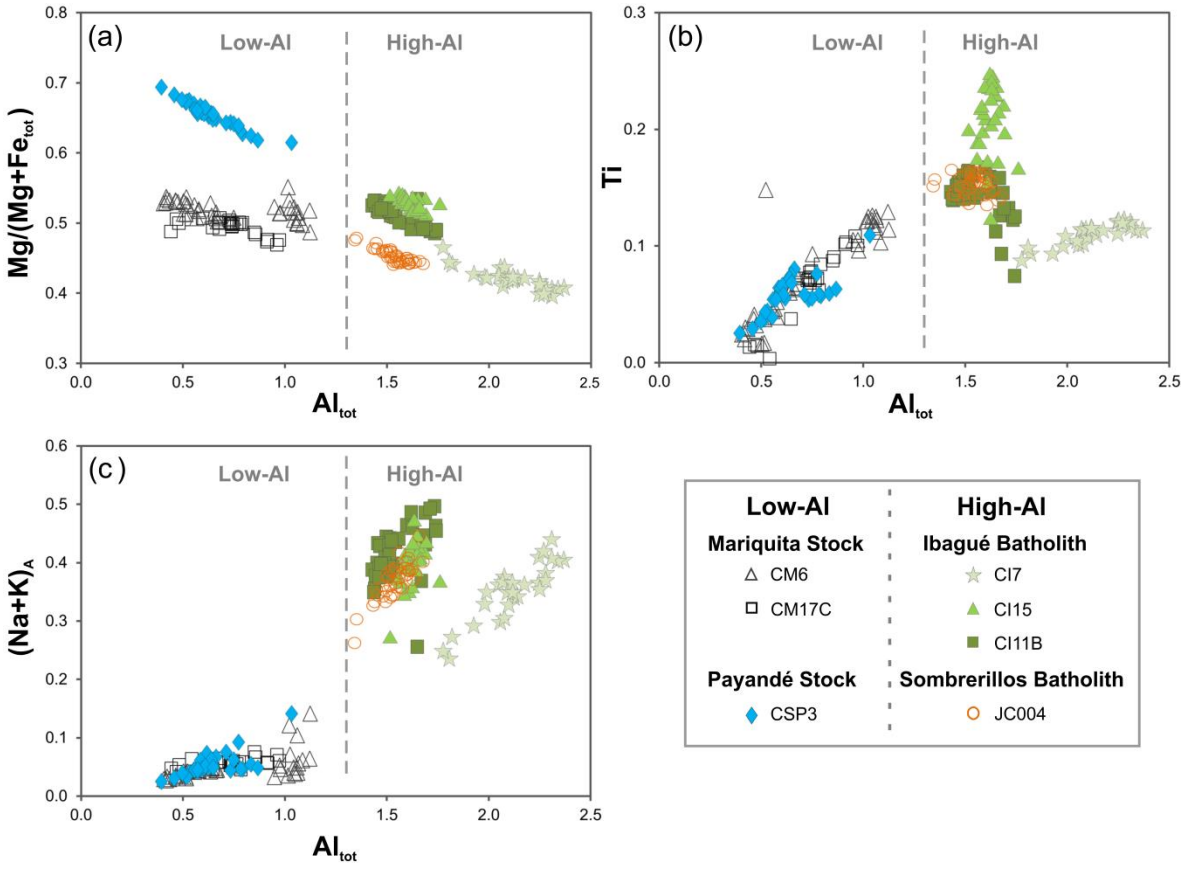

Figure 12. Compositional variations of amphibole in the Mariquita and Payandé Stocks, and Ibagué and Sombrerillos Batholiths. The low-Al and high-Al groups are separated in the figures by a dashed gray line. (a) Mg/(Mg+Fe$_{tot}$) vs. Al$_{tot}$. (b) Ti vs. Al$_{tot}$. (c) $(Na+K)_A$ vs. Al$_{tot}$.

We identified four types of amphiboles in the samples according to the Si and Al$_{tot}$ (apfu) composition variations trough the crystals (Figure 13). The more abundant are amphiboles with homogeneous compositions (33%) that show low compositional changes, followed by Si-poor core and Si-rich rim (29%). The least abundant are the Si-rich core and Si-poor rim

(25%) and the oscillatory amphiboles (13%). This last amphibole classification characterizes by multiple Si and Al_{tot} content variations throughout the crystals.

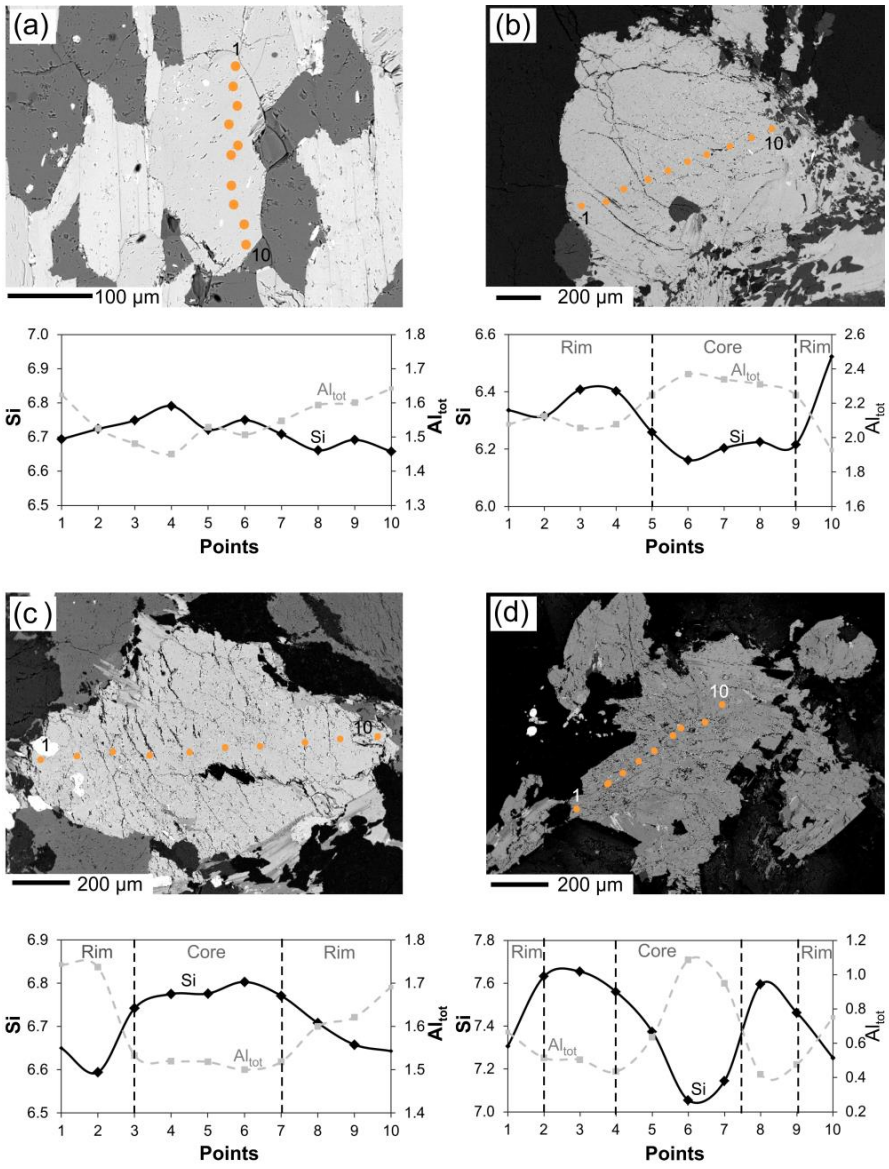

Figure 13. BSE images of the representative types of amphiboles and chemical variations. Si and Altot compositions along the crystal are plotted below each image. (a) Amphibole homogeneous (JC004-Sombrerillos Batholith). (b) Amphibole Si-poor core Si-rich rim (CI7- Ibagué Batholith). (c) Amphibole Si-rich core Si-poor rim (CI11B-Ibagué Batholith). (d) Amphibole with oscillatory Si compositions (CM6-Mariquita Stock). Altot behaves inversely to Si. Rim and core areas are marked in each profile and separated by the dashed lines.

4.4. Thermobarometry

The Al-in-hornblende barometer is calibrated with a determined mineral assemblage: quartz, K-feldspar, plagioclase, biotite, Fe-Ti oxides, titanite, and hornblende (Hammarstrom and Zen, 1986; Schmidt, 1992; Anderson and Smith, 1995). Most of our analyzed samples lack titanite, but according to Anderson and Smith (1995), it does not significantly affect pressure determinations. Some Ibagué Batholith samples contain clinopyroxene, however, it represents less than 2% of the mineralogical composition, and the Al content of amphibole is almost similar to that in samples with pyroxene absent.

The barometer must be applied to samples with plagioclase composition from An 25 to 35 (Anderson and Smith, 1995). In general, our samples roughly matched the recommended range, except for the samples CI15 and CI7 that have higher values (An34-52 and An 42-48, respectively). According to Anderson and Smith (1995), this slightly changes the hornblende Al content and, therefore, pressure, but we are going to take them as a reference. Also, the oxygen fugacity is another parameter to consider because high values give more reliable barometric results (Schmidt, 1992; Anderson and Smith, 1995). Therefore, we filtered the data and preserved data points only with $Fe^{3+/(}Fe^{3+}+Fe^{2+})>0.25$ in the Anderson and Smith (1995) analysis and >0.20 in the Schmidt (1992) and Mutch et al. (2016) measurements and selected samples with $Fe_{tot}/(Fe_{tot}+Mg)$ (#Fe) from 0.40 to 0.65. Payandé Stock sample (CSP3) has Fe# outside the application range and was not included in the calculations.

Pressure and temperature results show that Ibagué Batholith and Sombrerillos Batholith have the highest values compared with the Mariquita Stock (Fig 14a). Temperatures obtained range from 617.4 ±15.3 °C in the Mariquita Stock (CM17C-132 Ma) to 767.2 ± 9.2 °C in the Ibagué Batholith (CI15- 145.7 Ma). Pressure results obtained with the Anderson and Smith, (1995) calibration show that it decreases progressively from 5.0 kbar in the late Jurassic (Ibagué Batholith=152 Ma; 19.0 km depth) to 0.7 ± 0.5 - 2.0 ± 0.4 kbar in the middle Early Cretaceous (Mariquita Stock =132-130 Ma; 2.6 to 7.6 km depth) (Figure 14b). A peak pressure of 6.7 ± 0.5 kbar appears at 140 Ma (Ibagué Batholith-CI7;

25.5 km depth). The pressures calculated using the Schmidt (1992) and Mutch et al. (2016) calibrations show pressures ranging from 0.9 ±0.1 kbar at 130 Ma (CM6) to 8.0 ± 0.3 kbar at 140 Ma (CI7) (Table 5).

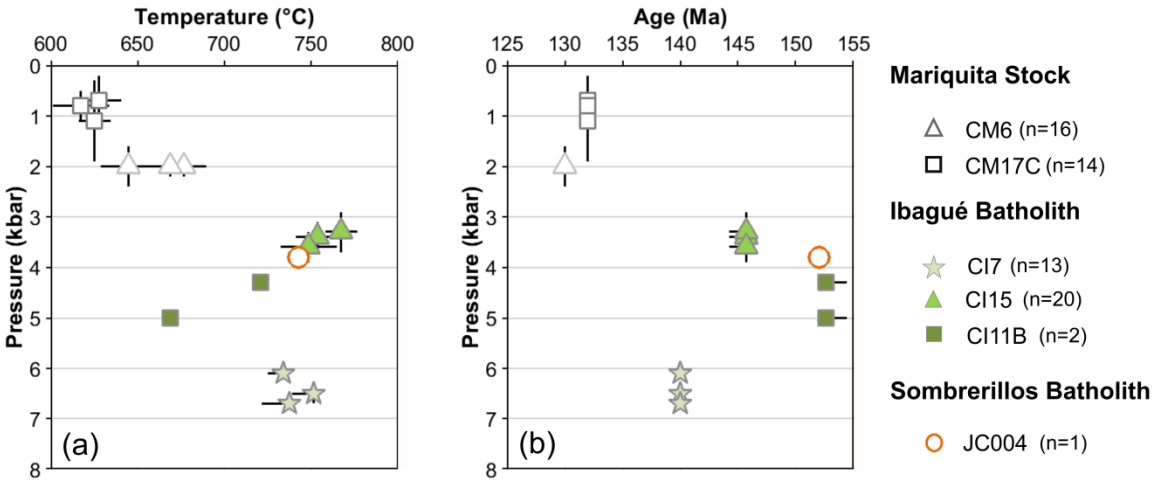

Figure 14. (a) Pressure (kbar) vs. temperature (°C) calculated for the Mariquita Stock, Ibagué Batholith, and Sombrerillos Batholith using the barometer of Anderson and Smith (1995) and the amphibole-plagioclase thermometer of Holland and Blundy (1994). (b) Pressure (kbar) vs. age (Ma). Each point with bars represents the average of several analyses in one amphibole crystal. Bars indicate 1σ error and n denote the number of analyses per sample; points with not bar display single analysis.

The differences between pressure results may be related to the barometer calibrations. The pressure is dependent on temperature and Schmidt (1992), and Mutch et al. (2016) barometers are calibrated with fixed temperature values equivalents to 655-700 °C and 725 ±75 °C, respectively. Additionally, Schmidt (1992) and Anderson and Smith (1995) are calibrated for pressures between 2.5 to 13 kbar, and they would be unsuitable for shallow intrusive rocks like Mariquita Stock. Mutch et al. (2016) would be more appropriated to calculate these pressures because it is calibrated for a 0.8 to 10 kbar range.

Table 5. Representative amphibole compositions from the Payandé and Mariquita Stocks and Ibagué and Sombrerillos Batholiths

	Payandé Stock	**Ibagué Batholith**						**Mariquita Stock**				**Sombrerillos Batholith**
Rock type	Granodiorite	Clinopyroxene-bearing diorite				Granodiorite		Granite				Granodiorite
Sample	CSP3	CI11B		CI15		CI7		CM17C		CM6		JC004
Analysis	2-6	3-1	4-3	1-7	3-1	1-9	3-4	1-2	2-5	1-6	3-6	2-4
(wt%)												
SiO_2	50.74	43.48	45.49	43.73	44.79	40.75	41.27	49.42	48.00	47.37	47.44	43.77
TiO_2	0.70	1.11	1.01	1.88	1.10	1.05	1.07	0.66	0.96	1.09	0.92	1.43
Al_2O_3	4.52	9.40	9.50	8.94	9.24	12.50	12.67	4.22	5.47	5.98	6.20	8.51
FeO*	14.03	18.15	16.92	16.61	16.72	20.36	19.64	19.06	19.76	18.79	18.75	19.56
MnO	0.60	0.42	0.39	0.39	0.45	0.68	0.67	0.91	0.81	0.79	0.87	1.09
MgO	13.92	10.24	10.85	10.92	10.89	7.60	7.49	10.49	9.77	10.72	10.40	8.63
CaO	11.42	11.50	11.18	11.09	11.27	11.57	11.25	10.80	10.47	10.47	10.40	10.93
Na_2O	0.97	1.05	1.03	1.44	1.30	1.18	1.23	0.78	1.01	1.11	1.06	1.35
K_2O	0.24	1.04	1.03	1.05	0.96	0.87	0.86	0.30	0.37	0.26	0.32	0.79
Cr_2O_3	0.02	0.00	0.04	0.01	0.00	0.02	0.01	0.00	0.00	0.12	0.08	0.01
Total	97.21	96.57	97.57	96.32	96.92	96.63	96.20	96.65	96.62	96.69	96.46	96.15
Formula calculated for 22 O												
Si	7.362	6.558	6.711	6.596	6.684	6.216	6.299	7.364	7.178	7.023	7.054	6.692
Ti	0.076	0.126	0.112	0.214	0.124	0.121	0.123	0.073	0.108	0.122	0.103	0.164
Al^{iv}	0.638	1.442	1.289	1.404	1.316	1.784	1.701	0.636	0.822	0.977	0.946	1.308
Al^{vi}	0.135	0.229	0.362	0.186	0.310	0.463	0.579	0.106	0.141	0.067	0.141	0.225
Cr	0.002	-	0.005	0.001	-	0.002	0.001	-	-	0.014	0.010	0.001
Fe^{2+}	1.221	1.554	1.411	1.513	1.490	1.824	1.844	1.723	1.724	1.370	1.422	1.883
Fe^{3+}	0.482	0.735	0.676	0.582	0.597	0.774	0.664	0.652	0.748	0.959	0.909	0.618
Mn	0.074	0.053	0.048	0.050	0.057	0.088	0.086	0.115	0.102	0.099	0.110	0.141
Mg	3.010	2.303	2.386	2.455	2.422	1.728	1.704	2.330	2.177	2.368	2.305	1.967
Ca	1.775	1.858	1.768	1.792	1.802	1.892	1.840	1.724	1.677	1.663	1.656	1.791
Na	0.272	0.309	0.293	0.422	0.375	0.350	0.364	0.225	0.293	0.319	0.306	0.399
K	0.045	0.201	0.194	0.201	0.182	0.169	0.167	0.057	0.070	0.049	0.061	0.153
OH	1.988	1.954	1.963	1.932	1.947	1.987	1.985	1.998	1.997	1.998	1.999	1.978
Cl	0.012	0.046	0.037	0.068	0.053	0.013	0.015	0.002	0.003	0.002	0.001	0.022
Al_{tot}	0.77	1.67	1.65	1.59	1.63	2.25	2.28	0.74	0.96	1.04	1.09	1.53
$(Na+K)_A$	0.09	0.37	0.26	0.42	0.36	0.41	0.37	0.06	0.07	0.05	0.06	0.34
$Mg/(Mg+Fe_{tot})$	0.64	0.50	0.53	0.54	0.54	0.40	0.40	0.50	0.47	0.50	0.50	0.44
$Fe^{3+}/(Fe^{3+}+Fe^{2+})$	0.28	0.32	0.32	0.28	0.29	0.30	0.26	0.27	0.30	0.41	0.39	0.25
X^{An} (plag)	22	31	31	37	37	44	44	21	21	24	24	29
PS92 (kbar)	-	4.9	4.8	4.6	4.7	7.7	7.8	-	-	-	-	4.3
PM16 (kbar)	-	-	-	-	-	-	-	1.3	1.7	1.9	2.0	-
PAS95 (kbar)	-	4.3	5	3.1	4.2	6.3	6.9	0.6	1.8	2	2.4	3.8
THB94 (°C)	-	721	669	769	720	752	730	614	633	675	651	715
Depth (km)	-	16.3	19.0	11.8	16.0	23.9	26.2	2.3	6.8	7.6	9.1	14.4

Note: X^{An} (plag) – mol % of anorthite. PS92 -Pressure calculated using Schmidt (1992). PM16-Pressure calculated using Mutch et al. (2016). PAS95- Pressure calculated using Anderson and Smith (1995). THB94- Temperature calculated using Holland and Blundy (1994). Depth – emplacement depth estimate from PAS95 (average crustal density is assumed as 2.7 g/cm^3; 1 kbar=3.8 km for the continental crust. Pressure calibration error= ±0.6 kbar and Temperature calibration error= ±40°C

4.5. Sr isotope composition

Whole-rock geochemistry, U-Pb ages, and Hf isotopes in zircon were previously reported by Bustamante et al. (2016) for the samples analyzed. The most felsic rock (CI7: 140 Ma) has an initial $^{87}Sr/^{86}Sr$ of 0.7049, whereas those that still preserves clinopyroxene (CI11A: 152 Ma) and clino- and orthopyroxene (CI9B: 142 Ma) yielded initial $^{87}Sr/^{86}Sr$ values of 0.7035 and 0.7036 respectively (Figure 15).

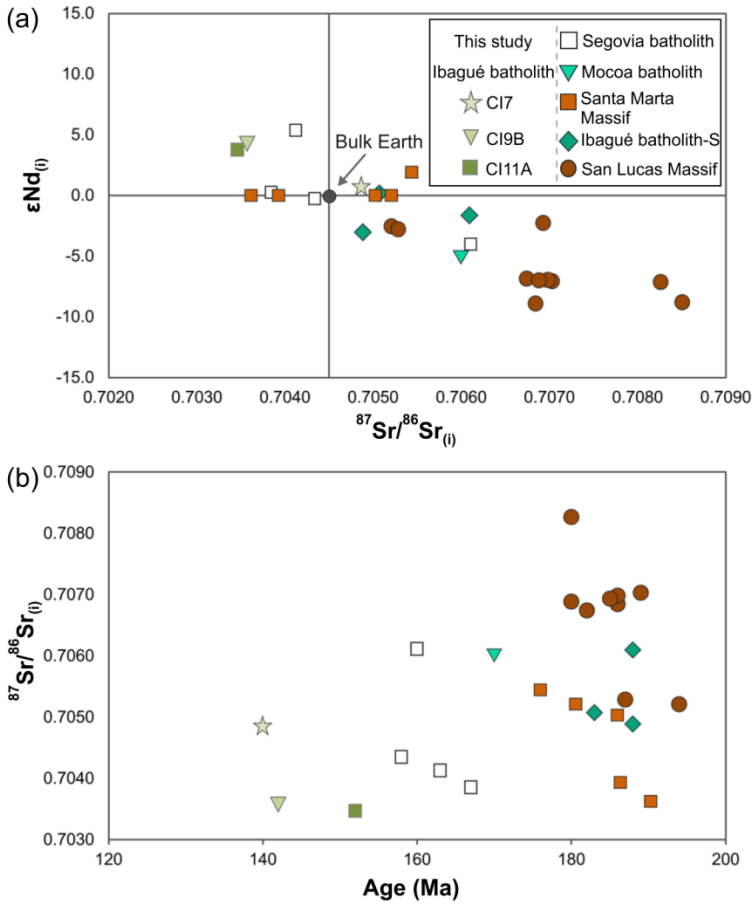

Figure 15. (a). Whole-rock initial εNd vs. initial 87Sr/86Sr for Jurassic to Early Cretaceous granitoids of the Central Cordillera of Colombia. (b) Initial $^{87}Sr/^{86}Sr$ vs. U-Pb ages (Ma). Data for Segovia batholith, Mocoa batholith, Ibagué Batholith South (S), and San Lucas Massif are from Leal-Mejia (2011) in Leal-Mejía et al. (2019) and Santa Marta Massif is from Quandt et al. (2018).

Figure 15 compares our data with Sr and Nd isotopes already reported in recent works (Quandt et al., 2018; Leal-Mejía et al., 2019) for the Jurassic magmatism in Colombia. Together, the Sr and Nd isotope signatures of the Jurassic magmatic rocks follow a mantle array trend, far from a depleted mantle source. Granitoids from San Lucas Massif are the oldest (194-178 Ma), and the most isotopically evolved with depleted εNd (mean= -6.0) and radiogenic $^{87}Sr/^{86}Sr$ (mean= 0.7069). The samples CI11A (152 Ma) and CI9B (142 Ma) are radiogenic (εNd= +3.7 and +4.2 respectively), whereas the youngest sample CI7 (140 Ma) plot close but shows more mixed sources (εNd= +0.8).

5. Discussion

5.1. Thermal constraints and fluid-fluxed melting

Considering that Zr and P_2O_5 diminished as differentiation increases, our results suggest that the Jurassic magmas of the Central Cordillera were zircon and apatite saturated (Figure 3). Our temperature estimates for the Jurassic magmatic rocks studied range from 674 to 778 °C and from 796 to 943 °C for zircon and apatite, respectively. Low Zr content (<300 ppm) in these arc-related rocks is similar to the contents reported in other calc-alkaline Cordilleran magmas (Collins et al., 2016). Additionally, anomalous values are not present in the zircon saturation temperatures of our samples, so zircon accumulation was not a significant process during magma evolution at the SiO_2 range (<64 wt%).

Temperatures estimated using Al in hornblende differed from those obtained with zircon saturation. For example, in the Mariquita Stock, the latter temperatures (724-757 °C) are higher than the former (617.4 ±15.3 °C), suggesting that saturation temperatures are inequivalent to magmatic or partial melting temperatures (Siégel et al., 2018). Instead, they indicate the temperature when the magma was Zr or P_2O_5 saturated and crystallized zircon or apatite, respectively (Bea et al., 1992; Siégel et al., 2018).

Even when both saturation temperatures have different values, the trend is the same, suggesting that similar processes modified the magma compositions (Whattam and Stern, 2016). We suggest that saturation conditions were likely controlled by the amount of fluids

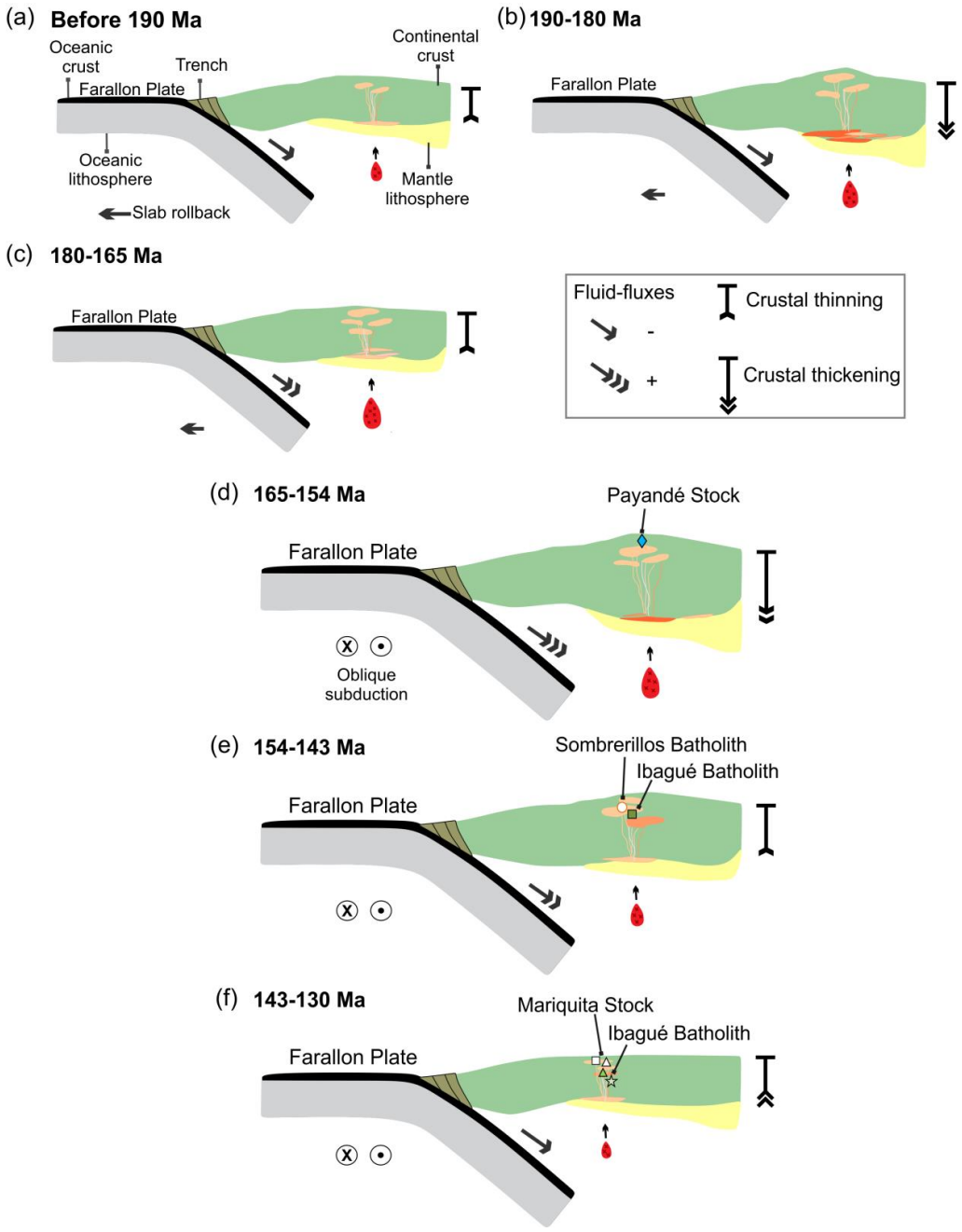

Figure 16. Schematic cross-section models showing the early Jurassic to early Cretaceous (before 190-130 Ma) crustal evolution of the subduction-related magmatic arc of the Northern Andes. Crustal thickness varied from 35 to 50 km throughout all the arc lifetime. During the Jurassic, the arc was mainly extensional, but two thickening episodes occurred. The first one during 190-180 Ma as a consequence of underplating during the onset of the slab rollback subduction and the last one during 165-154 Ma because of the tectonic shift toward oblique subduction. The maximum emplacement depths of the studied samples are located in the vertical section. The symbols are the same as Figure 12.

released from the slab as the subduction regime changed (Miller et al., 2003; Collins et al., 2016; Wang et al., 2017; Xie et al., 2018). Subduction onset, at the early Jurassic, has high saturation temperatures indicating that during that time, fluid fluxes in the melting were low (Figure 16).

We found that in the middle Jurassic at 165 Ma, the lowest saturation temperatures are recorded, which then progressively increased until the Early Cretaceous at 129 Ma. Low saturation temperatures suggest that in the middle Jurassic, a higher amount of fluids in the subducting slab triggered partial melting in the mantle wedge increasing the magma volumes (Collins et al., 2016); however, a continuous reduction in the fluid-fluxes diminished the magmatism at the shutdown of the subduction at the Early Cretaceous (Figure 16). This interpretation is consistent with the progressive decrease in the detrital zircon ages from 165 to 130 Ma reported by Bustamante et al. (2016), indicating that at that moment, magma production rates were diminishing. The variations during the middle Jurassic-early Cretaceous (165-130 Ma) are probably a consequence of the oblique subduction occurring during that time in the western margin of South America (Bayona et al., 2006; Blanco-Quintero et al., 2014; Bustamante et al., 2016). In this scenario, the variation in the convergence rate and the shallow angle subduction likely played a role in the progressive reduction of the fluids that reached the mantle wedge and, consequently in the magma volumes, as would be expected in this tectonic regimen (Sagong et al., 2005; Rooney et al., 2015).

5.2. Magma source depth and crustal thickness

Here we use our data to constrain the magma source depth and crustal thickness variations trough time in the Jurassic to Early Cretaceous (194-130 Ma) arc in the Central Cordillera in the Northern Andes. Our REE ratios and Sr/Y and $(La/Yb)_N$ crustal quantifications showed that it is possible to distinguish between thickening and thinning episodes (Figure 16) suggesting that crustal deformation processes such as those related with a slab rollback might not explain the whole crustal evolutionary history during the Jurassic in the Northern Andes.

This study shows that $(Dy/Yb)_N$ ratios decreased with differentiation during the Early Jurassic to Early Cretaceous, suggesting that amphibole was a significant fractionating and residual phase in the magmatic source (Romick et al., 1992; Macpherson et al., 2006; Davidson et al., 2007) mainly during the crustal thickening episodes of this magmatism. Additionally, the low Sm/Yb ratios, the flat HREE patterns, and the Eu decreasing with differentiation (Figures 3 and 4) also indicate that clinopyroxene and plagioclase might have been other important phases involved in the magmatic evolution. This interpretation indicates that in general, the magma sources during the 194-130 Ma in the Northern Andes evolved at low to medium pressures at depths likely between 35 to 50 km belonging to the field of magma equilibration with pyroxene and amphibole-bearing mineral residues (Kay et al., 1999; Kay and Mpodozis, 2001; Davidson et al., 2007). Granitoids of San Lucas Massif with crystallization ages from 194 to 182 Ma exhibited features such as low REE patterns steepness, more depleted light, and heavy REE, and a strong negative Eu anomaly. (Figure 4a and 5). These characteristics suggest that the older arc record (San Lucas Massif) of the subduction-related arc magmatism in the early Jurassic, the magma was fractionated at the lowest pressure (Kay et al., 1999; Mamani et al., 2010; Wörner et al., 2018). During that time, the magma likely experienced this process in a relatively thin crust at depths between 35 to 40 km (Figure 16) in the presence of residual mineral phases such as pyroxene and plagioclase as the REE ratios suggest. Spikings et al. (2019) proposed that a retreating oceanward subduction zone occurred during 209-194 Ma, suggesting that extensional processes dominated, and thus, a thin continental crust would be expected during that period. We suggest that another approach to explaining this thin crust during the early Jurassic may be the inheritance of the thin-crust formed during the extensional Triassic history. The high $^{87}Sr/^{86}Sr$ (mean= 0.7069) and low εNd (mean= -6.0) isotopes showed that granitoids of the San Lucas Massif are the most isotopically evolved. This feature might be explained by crustal assimilation either in a thicker or in an older crust (Chapman et al., 2017). These granitoids were emplaced in a Mesoproterozoic basement (Cuadros et al., 2014), and we suggest that the assimilation of this old continental crust might be the primary isotopic control rather than the assimilation in a thicker crust.

Even when the Sr/Y and $(La/Yb)_N$ estimation values differed between ratios, they recorded the same trends suggesting that the crust thickened during the 190-180 Ma and 160-154 Ma

intervals and was relatively thinned throughout 180-160 Ma and 154-143 Ma (Figure 6). Therefore, here we are going to analyze the thickening episodes and the mechanism that formed them. The first episode occurred from 190-180 Ma, and during this one, steeper REE patterns and high $(La/Yb)_N$ ratios characterized the granitoids belonging to Santa Marta Massif, Upper Magdalena Valley, and the Garzón Massif indicating that the magma fractionated at higher pressures and probably during an episode of crustal thickening (Kay et al., 1999, 2005) throughout the evolution of the subduction in the Northern Andes (Figure 16a). During this period, also the La/Sm and Sm/Yb ratios are higher, and the Eu anomaly is slightly developed or is absent. These features suggest that magmas during the 190 to 180 Ma fractionated inside the stability limit of equilibration with amphibole-bearing mineral residues and occasionally deeper than the plagioclase stability limit (Kay et al., 1999; Saleeby et al., 2003; Girardi et al., 2012; Winter, 2014). Previous studies of Santa Marta Massif granitoids (Quandt et al., 2018) using Sr/Y estimated that the crust was normal to moderately thickened (30-50 km) during the early Jurassic. These results are consistent with our REE ratios estimations for the early Jurassic (190-180 Ma) suggesting that when subduction started after 190 Ma, the crust began to increase its thickness to 40-50 km, likely due to crustal deformation processes such as shortening or magmatic processes such as basaltic underplating that may have contributed to an initial crustal thickening. This mechanism may have developed during a slab rollback setting as also have been evidenced in other magmatic arcs (Zhu et al., 2017; Zhou et al., 2018). Progressive slab rollback might have thinned the crust until ~165 Ma.

The second episode, according to the Sr/Y and $(La/Yb)_N$ quantifications and the behavior of the REE ratios may have occurred during the 160 to 154 Ma in the southern segment (Payandé Stock, Ibagué Batholith and Segovia Batholith), when the crust was thickened to ~40 to 50 km (Figure 16d). Leal-Mejía et al. (2019) suggested that during this period, the granitoids were emplaced in a neutral to compressive tectonic regime due to the absence of coeval volcanism. Therefore, the tectonic evolution of the arc was complex, and the mechanism of the slab rollback subduction is not enough to explain the history of the arc after the middle to late Jurassic (165-130 Ma), where a more compressive character is present. Crustal thickening during this time would be explained by the change in the

subduction history where variations in the slab dip or the angle of convergence might have deformed the crust.

Blanco-Quintero et al. (2014), based on the geochronology of amphibolites and pelitic schist of the Cajamarca Complex, suggested that a metamorphic event occurred between 158-146 Ma as a consequence of the collisional event documented in the Northern Andes in the middle to late Jurassic. The event has been recorded mainly at the south of the arc as a consequence of an oblique subduction setting, which may have produced the medium P-T regional metamorphism of the Cajamarca Complex, located in faulted contact to the east with the Ibagué Batholith (Bayona et al., 2006; Blanco-Quintero et al., 2014). However, recent studies would let to extend this period since 164 Ma in regions in the southern segment of the arc (Zapata-García et al., 2017; Bustamante et al., 2017). The tectonic shortening evidenced by the metamorphism is one possible evidence of the oblique subduction at the NW margin of South America that has produced an increase in the crustal thickness (De Saint Blanquat et al., 1998) as suggested by the REE ratios.

For the late Jurassic, Bustamante, et al. (2016), using Sr/Y estimated that the crust was normal to relatively thin (25-45 km). This result is consistent with our data after 154 Ma that indicates that the crust became progressively thinner toward the early Cretaceous (130 Ma), reaching a crustal thickness likely from 35 to 40 km, as was suggested by the magma source depths. The early Cretaceous Mariquita Stock (134-130 Ma) shows similar geochemical characteristics than those of the San Lucas Massif, such as low REE patterns steepness, more depleted light, and heavy REE, and a strong negative Eu anomaly (Figure 4h and 5). These features indicate that during the final episodes of the subduction-related arc magmatism, the magma was fractionated at a lower pressure (Kay et al., 1999; Mamani et al., 2010; Wörner et al., 2018) and in a thin crust (~35-40 km) as occurred during the Early Jurassic (Figure 16f).

5.3. Emplacement conditions during the final episodes of the Northern Andes arc magmatism

As argued above, the Jurassic magmatic arc of the Northern Andes experienced changes in the magma source depth, crustal thickness, temperatures, and fluid fluxes, throughout its evolution. During the period between 165-130 Ma occurred the final episodes of the magmatism in this arc in the central-southern segment in the Central Cordillera (Payandé Stock, Segovia Batholith, Ibagué Batholith, and Mariquita Stock). Between 165-154 Ma, the crust underwent a thickening episode (40-50 km) related to a shift to an oblique subduction regime that occurred in the middle Jurassic (Figure 16d). This episode included an increase in the amount of fluid-fluxes and moderate magmatism. Afterward, in the zone of Ibagué batholith and Mariquita Stock, from 154 to 130 Ma, the crust was thinner (35-40 km), likely due to variations in the parameters of the oblique subduction and the progressive decrease in the fluid and magmatic contribution (Figure 16e-f). The granitoids of the southern segment of the arc represented by the Ibagué and Sombrerillos batholiths and Payandé and Mariquita stocks (Figure 2) were emplaced in this tectonic scenario during the middle Jurassic to Early Cretaceous (165-130 Ma), and the implications of the emplacement conditions in this last stage of the arc will be discussed below. This segment was selected for more detailed analyses because it is part of a more coherent and less complex tectonic block.

Amphibole crystallization pressures between 6.7 ±0.5 kbar at 140 Ma to 0.7 ±0.5 kbar at 132 Ma(Figure 14) indicate emplacement depths from 25.5 km to 2.6 km suggesting that Sombrerillos and Ibagué batholiths were emplaced at the middle to deep crustal levels during the late Jurassic to early Cretaceous (ca. 153-140 Ma) and the Mariquita Stock emplaced shallower in the crust at the middle early Cretaceous (132-130 Ma). Additionally, the plutons that recorded higher pressures also displayed higher temperatures (maximum 767.2 ±9.2 °C) compared with the Mariquita Stock (minimum 617.4 ±15.3 °C) that showed temperatures below the solidus in a water-saturated magma (<650°C; Castro, 2013) which would be expected for low-pressure emplacements. We suggest that Payandé Stock has similar emplacement conditions to Mariquita Stock, and it was emplaced in the middle Jurassic (165 Ma) also at shallow crustal levels and low temperatures. It is evidenced by the similar amphibole chemical compositions where low Al_{tot} contents characterized both stocks.

Previous studies on the Jurassic magmatism in the Northern Andes (Aspden et al., 1987; Bustamante et al., 2010, 2016; Cochrane et al., 2014; Spikings et al., 2015; Quandt et al., 2018; Rodríguez et al., 2018; Leal-Mejía et al., 2019) have not reported thermobarometric estimations that let us compare the pressures and temperatures obtained in this work. However, relative estimations have suggested that magmas in the Ibagué Batholith were emplaced at shallow levels on the crust based on field evidence such as the limited contact metamorphism (Aspden et al., 1987) and the lack of associations with effusive and explosive volcanic rocks (Bustamante et al., 2010). However, as stated above, emplacement level depths are variable, and the batholiths are emplaced deeper in the crust compared with stocks (Figure 17).

Otú-Pericos and Ibagué faults have been considered as the major fault systems in the Ibagué Batholith and a possible mechanism for magma transporting and emplacement (Aspden et al., 1987; Bustamante et al., 2017; Quandt et al., 2018). Therefore, faults may be an option to explain the pressure variations where it would be expected that the rocks closer to the major faults have the highest pressures as a consequence of processes such as uplift or exhumation during the emplacement (Margirier et al., 2016). Nevertheless, our data show a scatter pattern respect to the distance to major faults (Figure 2), and additionally, the studied samples do not evidence syntectonic intrusion features (Bustamante et al., 2016). Thus, we suggest that the deeper emplacement depths are uncorrelated with the distance from faults, and consequently, they are not likely controlling the magmatic pressures. Analysis of the structural emplacement conditions in the southern segment of the arc is out of the scope of this study, and further studies are necessary to constrain the role of the faults accurately.

As argued above, the last stage of magmatism in this arc is characterized by the emplacement at higher pressures, that in the late Jurassic are slightly lower but similar to the pressures reported by Blanco-Quintero et al. (2014) for the metamorphic units (550-580°C and 8 kbar). In the north segment of the Ibagué Batholith, some samples displayed petrographic features such as oriented mafic minerals and quartz with deformation textures

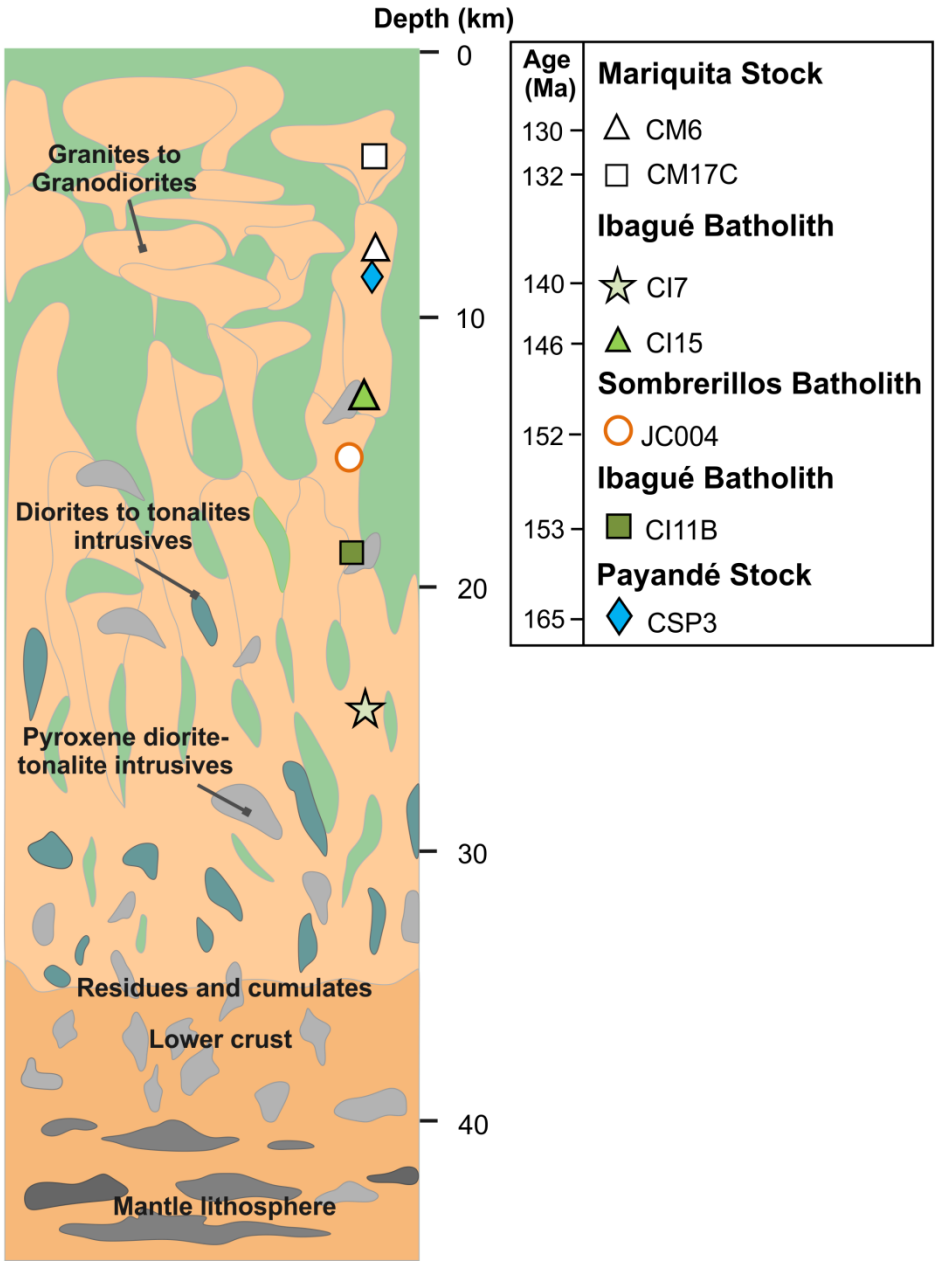

Figure 17. Schematic vertical section of a continental arc from the surface until the top of the arc root (modified from Ducea et al., 2015). The studied rocks of the Ibagué and Sombrerillos batholiths and Mariquita and Payandé stocks are located at the maximum emplacement depth for each sample. The emplacement conditions varied from ~3 to 25 km during 165 Ma to 130 Ma in the Northern Andes. The batholiths emplaced deeper than the stocks reaching depths close to the arc roots in the Ibagué Batholith at 140 Ma (25.5 km)..

like subgrain rotation or grain boundary migration (Figure 7f) that might evidence incipient solid-state deformation at high-temperature conditions (Moyen et al., 2003). These

characteristics are expected at deeper levels in the crust in obliquely convergent settings (De Saint Blanquat et al., 1998; Moyen et al., 2003). Another process recorded during the construction of the plutons in the last magmatic episode was the amalgamation of various pulses. This event is best recorded in the Ibagué Batholith (152-140 Ma), where a mafic pulse was injected in the magma. It is evidenced in the mineralogy were samples showed features related to more mafic compositions such as the presence of clinopyroxenes in some samples and the more Ca- and Mg-rich plagioclases and amphiboles, respectively (Figure 8 and 11). Additionally, enclaves (sample CI9B) characterized by more mafic mineralogy and coronitic texture of amphibole and ortho- and clinopyroxenes (Figure 7e) suggest that they are a consequence of mafic pulses and likely were formed during magma mingling (Bellos et al., 2015). Furthermore, amphibole zonation patterns (Figure 13) and the poikilitic texture (Figure 7) indicate that another process occurred during the magmatic pulses related to the mixing of magmas at two or more crystallization stages and variable pressures, besides of Si-rich post-magmatic overgrowth in some samples.

6. Conclusions

Early Jurassic to Early Cretaceous subduction-related arc crust in the Northern Andes in Colombia underwent two thickening episodes related to tectonic events during the 190 to180 Ma and 165 to 154 Ma. During the arc lifetime, the crust varied in thickness from 35 to 50 km, and the primary residual source was amphibole, but plagioclase and pyroxene were also secondary phases involved during the magma genesis. Before 190 Ma, the crust was relatively thin (35-40 km), as suggested by the REE features of granitoids from San Lucas Massif. Afterward, in the early Jurassic, during the onset of the subduction slab rollback, the crust became thicker (40-50 km), likely due to a basaltic underplating process. Progressive slab rollback thinned the crust, increased the magmatic volumes, and reduced the fluid-fluxes. This tectonic setting changed during the middle Jurassic when the subduction parameters changed, and a collisional event occurred in the southern part of the arc as a result of the oblique subduction of the Farallon plate with the SW margin of South America. Consequently, the crust underwent a thickening episode from 165 to 154 Ma and might have been thickened until ˜50 km; progressively, the fluid fluxes and the magmatic

volumes began to decrease as suggested by the saturation temperatures. At the beginning of this thickening period (165 Ma), the Payandé Stock was emplaced at low temperature and shallow crustal level conditions.

After 154 Ma and until the Early Cretaceous (130 Ma), the crust was continuously thinned (35-40 km). From 154 to 140 Ma, Sombrerillos and Ibagué batholiths were emplaced at the middle to deep crustal levels, at maximum pressures and temperatures of 6.7 ±0.5 kbar (maximum crustal depth= 25.5 km) and 767.6 ±9.2 °C, respectively. Major faults such as Otú-Pericos and Ibagué might have played a significant role in the transport and emplacement of the magmas, but they are not likely controlling the highest pressures.

During the last stage of the magmatism, in the southern segment, the petrography and mineral chemistry recorded processes that occurred during the construction of the plutons, such as solid-state deformation at high-temperature conditions at deeper levels in the crust likely as a consequence of the obliquely convergent setting. A mafic pulse was injected in the magma mainly in the north of the Ibagué Batholith, modifying the mineralogy and forming enclaves throughout mingling processes. Furthermore, the mixing of two or more crystallization magmatic stages at different pressures is another process.

In the Early Cretaceous, the Mariquita Stock was emplaced at low pressures and temperatures in shallower crustal levels compared with the previous plutons. It represents the last pulse of the magmatism in a thinner crust (~35 km).

7. Acknowledgments

This study was funded by the Vicerrectoria de Descubrimiento y Creación of Universidad EAFIT and it is part of the project "Evolución del magmatismo de arco Jurásico de la Cordillera Central de Colombia y su relación con la tectónica Mesozoica de los Andes del Norte" (851-000016, 828-000061 and 881-000071). Additionally, the authors were supported by the Society of Economic Geologist (SEG) grant SRG 19-128. Authors are grateful to D. Godoy for providing support in the acquisition of mineral chemistry data and M. Restrepo for valuable comments. This is a contribution to the Semillero de Investigación en Mineralogía y Petrología of EAFIT University.

8. Supplementary data

Readers can access the data supporting the analysis in this study in the Supplementary Data Tables 1-5.

9. References

Anderson, J.L., Barth, A.P., Wooden, J.L., Mazdab, F., 2008. Thermometers and thermobarometers in granitic systems. Rev. Mineral. Geochemistry 69, 121–142. doi:10.2138/rmg.2008.69.4

Anderson, J.L., Smith, D.R., 1995. The effects of temperature and fO_2 on the Al-in-hornblende barometer. Am. Mineral. 80, 549–559.

Aspden, J.A., McCourt, W.J., Brook, M., 1987. Geometrical control of subduction-related magmatism: the Mesozoic and Cenozoic plutonic history of western Colombia. J. Geol. Soc. London. 144, 893–905. doi:10.1144/gsjgs.144.6.0893

Bayona, G., Bustamante, C., Nova, G., Salazar-Franco, A.M., 2020. Jurassic evolution of the northwestern corner of Gondwana: Present knowledge and future challenges in studying Colombian Jurassic rocks, in: Gómez, J., Pinilla-Pachon, A.O. (Eds.), The Geology of Colombia. Bogotá, p. 37. doi:10.32685/pub.esp.36.2019.05

Bayona, G., Jiménez, G., Silva, C., Cardona, A., Montes, C., Roncancio, J., Cordani, U., 2010. Paleomagnetic data and K–Ar ages from Mesozoic units of the Santa Marta massif: A preliminary interpretation for block rotation and translations. J. South Am. Earth Sci. 29, 817–831. doi:10.1016/j.jsames.2009.10.005

Bayona, G., Rapalini, A.E., Costanzo-Alvarez, V., 2006. Paleomagnetism in Mesozoic rocks of the Northern Andes and its implications in Mesozoic tectonics of northwestern South America. Earth, Planets Sp. 58, 1255–1272. doi:10.1186/BF03352621

Bea, F., Fershtater, G., Corretgé, L.G., 1992. The geochemistry of phosphorus in granite rocks and the effect of aluminium. Lithos 29, 43–56. doi:10.1016/0024-4937(92)90033-U

Bellos, L.I., Castro, A., Díaz-Alvarado, J., Toselli, A., 2015. Multi-pulse cotectic evolution and in-situ fractionation of calc-alkaline tonalite–granodiorite rocks, Sierra de Velasco batholith, Famatinian belt, Argentina. Gondwana Res. 27, 258–280. doi:10.1016/j.gr.2013.09.019

Blanco-Quintero, I.F., García-Casco, A., Toro, L.M., Moreno, M., Ruiz, E.C., Vinasco, C.J., Cardona, A., Lázaro, C., Morata, D., 2014. Late Jurassic terrane collision in the northwestern margin of Gondwana (Cajamarca Complex, eastern flank of the Central Cordillera, Colombia). Int. Geol. Rev. 56, 1852–1872. doi:10.1080/00206814.2014.963710

Boehnke, P., Watson, E.B., Trail, D., Harrison, T.M., Schmitt, A.K., 2013. Zircon saturation re-revisited. Chem. Geol. 351, 324–334. doi:10.1016/j.chemgeo.2013.05.028

Bustamante, A., Juliani, C., Essene, E.J., Hall, C.M., Hyppolito, T., 2012. Geochemical constraints on blueschist- and amphibolite-facies rocks of the Central Cordillera of Colombia: the Andean Barragán region. Int. Geol. Rev. 54, 1013–1030. doi:10.1080/00206814.2011.594226

Bustamante, A., Juliani, C., Hall, C.M., Essene, E.J., 2011. 40Ar/39Ar ages from blueschists of the Jambaló region, Central Cordillera of Colombia: Implications on the styles of accretion in the Northern Andes. Geol. Acta 9, 351–362. doi:10.1344/105.000001697

Bustamante, C., Archanjo, C.J., Cardona, A., Bustamante, A., Valencia, V.A., 2017. U-Pb ages and Hf isotopes in zircons from parautochthonous Mesozoic terranes in the Western margin of Pangea: Implications for the terrane configurations in the Northern Andes. J. Geol. 125, 487–500. doi:10.1086/693014

Bustamante, C., Archanjo, C.J., Cardona, A., Vervoort, J.D., 2016. Late Jurassic to Early Cretaceous plutonism in the Colombian Andes: A record of long-term arc maturity.

Geol. Soc. Am. Bull. 128, 1762–1779. doi:10.1130/B31307.1

Bustamante, C., Cardona, A., Bayona, G., Mora, A., Valencia, V., Gehrels, G., Vervoort, J., 2010. U-Pb LA-ICP-MS geochronology and regional correlation of Middle Jurassic intrusive rocks from the Garzon Massif, Upper Magdalena Valley and Central Cordillera, Southern Colombia. Bol. Geol. 32, 93–110.

Castro, A., 2013. Tonalite–granodiorite suites as cotectic systems: A review of experimental studies with applications to granitoid petrogenesis. Earth-Science Rev. 124, 68–95. doi:10.1016/j.earscirev.2013.05.006

Cediel, F., Shaw, R.P., Cáceres, C., 2003. Tectonic assembly of the Northern Andean Block, in: Bartolini, C., Buffler, R.T., Blickwede, J. (Eds.), The Circum-Gulf of Mexico and the Caribbean: Hydrocarbon Habitats, Basin Formation, and Plate Tectonics. pp. 815–848.

Chapman, J.B., Ducea, M.N., DeCelles, P.G., Profeta, L., 2015. Tracking changes in crustal thickness during orogenic evolution with Sr/Y: An example from the North American Cordillera. Geology 43, 919–922. doi:10.1130/G36996.1

Chapman, J.B., Ducea, M.N., Kapp, P., Gehrels, G.E., DeCelles, P.G., 2017. Spatial and temporal radiogenic isotopic trends of magmatism in Cordilleran orogens. Gondwana Res. 48, 189–204. doi:10.1016/j.gr.2017.04.019

Chiaradia, M., 2015. Crustal thickness control on Sr/Y signatures of recent arc magmas: an Earth scale perspective. Sci. Rep. 5, 8115. doi:10.1038/srep08115

Cochrane, R., Spikings, R., Gerdes, A., Winkler, W., Ulianov, A., Mora, A., Chiaradia, M., 2014. Distinguishing between in-situ and accretionary growth of continents along active margins. Lithos 202–203, 382–394. doi:10.1016/j.lithos.2014.05.031

Collins, W.J., Huang, H.Q., Jiang, X., 2016. Water-fluxed crustal melting produces Cordilleran batholiths. Geology 44, 143–146. doi:10.1130/G37398.1

Cuadros, F.A., Botelho, N.F., Ordóñez-Carmona, O., Matteini, M., 2014. Mesoproterozoic crust in the San Lucas Range (Colombia): An insight into the crustal evolution of the northern Andes. Precambrian Res. 245, 186–206.

doi:10.1016/j.precamres.2014.02.010

Davidson, J., Turner, S., Handley, H., Macpherson, C., Dosseto, A., 2007. Amphibole "sponge" in arc crust? Geology 35, 787. doi:10.1130/G23637A.1

De Saint Blanquat, M., Tikoff, B., Teyssier, C., Vigneresse, J.L., 1998. Transpressional kinematics and magmatic arcs. Geol. Soc. London, Spec. Publ. 135, 327–340. doi:10.1144/GSL.SP.1998.135.01.21

Ducea, M.N., Saleeby, J.B., Bergantz, G., 2015. The Architecture, Chemistry, and Evolution of Continental Magmatic Arcs. Annu. Rev. Earth Planet. Sci. 43, 299–331. doi:10.1146/annurev-earth-060614-105049

Farner, M.J., Lee, C.-T.A., 2017. Effects of crustal thickness on magmatic differentiation in subduction zone volcanism: A global study. Earth Planet. Sci. Lett. 470, 96–107. doi:10.1016/j.epsl.2017.04.025

Gaschnig, R.M., Vervoort, J.D., Lewis, R.S., Tikoff, B., 2011. Isotopic evolution of the Idaho batholith and Challis intrusive province, Northern US Cordillera. J. Petrol. 52, 2397–2429. doi:10.1093/petrology/egr050

Girardi, J.D., Patchett, P.J., Ducea, M.N., Gehrels, G.E., Cecil, M.R., Rusmore, M.E., Woodsworth, G.J., Pearson, D.M., Manthei, C., Wetmore, P., 2012. Elemental and isotopic evidence for granitoid genesis from deep-seated sources in the Coast Mountains Batholith, British Columbia. J. Petrol. 53, 1505–1536. doi:10.1093/petrology/egs024

Hammarstrom, J.M., Zen, E.-A., 1986. Aluminum in hornblende: An empirical igneous geobarometer. Am. Mineral. 71, 1297–1313.

Harrison, T.M., Watson, E.B., 1984. The behavior of apatite during crustal anatexis: Equilibrium and kinetic considerations. Geochim. Cosmochim. Acta 48, 1467–1477. doi:10.1016/0016-7037(84)90403-4

Hincapié-Gómez, S., Cardona, A., Jiménez, G., Monsalve, G., Ramírez-Hoyos, L., Bayona, G., 2018. Paleomagnetic and gravimetrical reconnaissance of Cretaceous volcanic rocks from the Western Colombian Andes: paleogeographic connections with the

Caribbean Plate. Stud. Geophys. Geod. 62, 485–511. doi:10.1007/s11200-016-0678-y

Holland, T., Blundy, J., 1994. Non-ideal interactions in calcic amphiboles and their bearing on amphibole-plagioclase thermometry. Contrib. to Mineral. Petrol. 116, 433–447. doi:10.1007/BF00310910

Jaramillo, J.S., Cardona, A., León, S., Valencia, V., Vinasco, C., 2017. Geochemistry and geochronology from Cretaceous magmatic and sedimentary rocks at 6°35′ N, western flank of the Central cordillera (Colombian Andes): Magmatic record of arc growth and collision. J. South Am. Earth Sci. 76, 460–481. doi:10.1016/j.jsames.2017.04.012

Ji, W.Q., Wu, F.Y., Chung, S.L., Liu, C.Z., 2014. The Gangdese magmatic constraints on a latest Cretaceous lithospheric delamination of the Lhasa terrane, southern Tibet. Lithos 210–211, 168–180. doi:10.1016/j.lithos.2014.10.001

Kay, S.M., Godoy, E., Kurtz, A., 2005. Episodic arc migration, crustal thickening, subduction erosion, and magmatism in the south-central Andes. Geol. Soc. Am. Bull. 117, 67. doi:10.1130/B25431.1

Kay, S.M., Mpodozis, C., 2001. Central Andean Ore Deposits Linked to Evolving Shallow Subduction Systems and Thickening Crust. GSA Today 11, 4. doi:10.1130/1052-5173(2001)011<0004:CAODLT>2.0.CO;2

Kay, S.M., Mpodozis, C., Coira, B., 1999. Neogene Magmatism, Tectonism, and Mineral Deposits of the Central Ande (22° to 33° S Latitude), in: Geology and Ore Deposits of the Central Andes. Society of Economic Geologists. doi:10.5382/SP.07.02

Kerr, A.C., Marriner, G.F., Tarney, J., Nivia, A., Saunders, A.D., Thirlwall, M.F., Sinton, C.W., 1997. Cretaceous Basaltic Terranes in Western Colombia: Elemental, Chronological and Sr-Nd Isotopic Constraints on Petrogenesis. J. Petrol. 38, 677–702. doi:10.1093/petroj/38.6.677

Leake, B.E., Woolley, A.R., Arps, C.E.S., Birch, W.D., Gilbert, M.C., Grice, J.D., Hawthorne, F.C., Kato, A., Kisch, H.J., Krivovichev, V.G., Linthout, K., Laird, J., Mandarino, J.A., Maresch, W. V., Nickel, E.H., Rock, N.M.S., Schumacher, J.C., Smith, D.C., Stephenson, N.C.N., Ungaretti, L., Whittaker, E.J.W., Youzhi, G., 1997.

Nomenclature of amphiboles: Report of the subcommittee on amphiboles of the international mineralogical association, commission on new minerals and mineral names. Am. Mineral. 82, 1019–1037. doi:10.1180/minmag.1997.061.405.13

Leal-Mejía, H., 2011. Phanerozoic Gold Metallogeny in the Colombian Andes: A Tectono-Magmatic Approach. Tesis Dr. Universitat de Barcelona.

Leal-Mejía, H., Shaw, Robert P., Melgarejo i Draper, J.C., 2019. Spatial-temporal migration of granitoid magmatism and the phanerozoic tectono-magmatic evolution of the Colombian Andes, in: Cediel, F., Shaw, Robert Peter (Eds.), Geology and Tectonics of Northwestern South America: The Pacific-Caribbean-Andean Junction. Springer, pp. 253–410. doi:10.1007/978-3-319-76132-9_5

Li, C., Wang, Z., Wang, D., Cao, W., Yu, X., Zhou, G., Gao, W., 2014. Crust-mantle interaction triggered by oblique subduction of the Pacific plate: Geochronological, geochemical, and Hf isotopic evidence from the Early Cretaceous volcanic rocks of Zhejiang Province, southeast China. Int. Geol. Rev. 56, 1732–1753. doi:10.1080/00206814.2014.956347

Macpherson, C.G., Dreher, S.T., Thirlwall, M.F., 2006. Adakites without slab melting: High pressure differentiation of island arc magma, Mindanao, the Philippines. Earth Planet. Sci. Lett. 243, 581–593. doi:10.1016/j.epsl.2005.12.034

Mamani, M., Worner, G., Sempere, T., 2010. Geochemical variations in igneous rocks of the Central Andean orocline (13 S to 18 S): Tracing crustal thickening and magma generation through time and space. Geol. Soc. Am. Bull. 122, 162–182. doi:10.1130/B26538.1

Margirier, A., Audin, L., Robert, X., Herman, F., Ganne, J., Schwartz, S., 2016. Time and mode of exhumation of the Cordillera Blanca batholith (Peruvian Andes). J. Geophys. Res. Solid Earth 121, 6235–6249. doi:10.1002/2016JB013055

Marshall, D., 1996. Ternplot: An excel spreadsheet for ternary diagrams. Comput. Geosci. 22, 697–699. doi:10.1016/0098-3004(96)00012-X

Matzel, J.E.P., Bowring, S.A., Miller, R.B., 2006. Time scales of pluton construction at

differing crustal levels: Examples from the Mount Stuart and Tenpeak intrusions, North Cascades, Washington. Geol. Soc. Am. Bull. 118, 1412–1430. doi:10.1130/B25923.1

McDonough, W.F., Sun, S. s., 1995. The composition of the Earth. Chem. Geol. 120, 223–253. doi:10.1016/0009-2541(94)00140-4

Miller, C.F., McDowell, S.M., Mapes, R.W., 2003. Hot and cold granites? Implications of zircon saturation temperatures and preservation of inheritance. Geology 31, 529. doi:10.1130/0091-7613(2003)031<0529:HACGIO>2.0.CO;2

Mora, A., Gaona, T., Kley, J., Montoya, D., Parra, M., Quiroz, L.I., Reyes, G., Strecker, M.R., 2009. The role of inherited extensional fault segmentation and linkage in contractional orogenesis: a reconstruction of Lower Cretaceous inverted rift basins in the Eastern Cordillera of Colombia. Basin Res. 21, 111–137. doi:10.1111/j.1365-2117.2008.00367.x

Moyen, J.-F., Nédélec, A., Martin, H., Jayananda, M., 2003. Syntectonic granite emplacement at different structural levels: the Closepet granite, South India. J. Struct. Geol. 25, 611–631. doi:10.1016/S0191-8141(02)00046-9

Mutch, E.J.F., Blundy, J.D., Tattitch, B.C., Cooper, F.J., Brooker, R.A., 2016. An experimental study of amphibole stability in low-pressure granitic magmas and a revised Al-in-hornblende geobarometer. Contrib. to Mineral. Petrol. 171, 85. doi:10.1007/s00410-016-1298-9

Profeta, L., Ducea, M.N., Chapman, J.B., Paterson, S.R., Gonzales, S.M.H., Kirsch, M., Petrescu, L., DeCelles, P.G., 2015. Quantifying crustal thickness over time in magmatic arcs. Sci. Rep. 5, 1–7. doi:10.1038/srep17786

Quandt, D., Trumbull, R.B., Altenberger, U., Cardona, A., Romer, R.L., Bayona, G., Ducea, M., Valencia, V., Vásquez, M., Cortes, E., Guzman, G., 2018. The geochemistry and geochronology of Early Jurassic igneous rocks from the Sierra Nevada de Santa Marta, NW Colombia, and tectono-magmatic implications. J. South Am. Earth Sci. 86, 216–230. doi:10.1016/j.jsames.2018.06.019

Ramos, V.A., 2009. Anatomy and global context of the Andes: Main geologic features and the Andean orogenic cycle, in: Backbone of the Americas: Shallow Subduction, Plateau Uplift, and Ridge and Terrane Collision. Geological Society of America, pp. 31–65. doi:10.1130/2009.1204(02)

Ridolfi, F., Renzulli, A., 2012. Calcic amphiboles in calc-alkaline and alkaline magmas: Thermobarometric and chemometric empirical equations valid up to 1,130°C and 2.2 GPa. Contrib. to Mineral. Petrol. 163, 877–895. doi:10.1007/s00410-011-0704-6

Rodríguez, G., Arango, M.I., Zapata, G., Bermúdez, J.G., 2018. Petrotectonic characteristics, geochemistry, and U-Pb geochronology of Jurassic plutons in the Upper Magdalena Valley-Colombia: Implications on the evolution of magmatic arcs in the NW Andes. J. South Am. Earth Sci. 81, 10–30. doi:10.1016/j.jsames.2017.10.012

Romick, J.D., Kay, S.M., Kay, R.W., 1992. The influence of amphibole fractionation on the evolution of calc-alkaline andesite and dacite tephra from the central Aleutians, Alaska. Contrib. to Mineral. Petrol. 112, 101–118. doi:10.1007/BF00310958

Rooney, T.O., Morell, K.D., Hidalgo, P., Fraceschi, P., 2015. Magmatic consequences of the transition from orthogonal to oblique subduction Panama. Geochemistry, Geophys. Geosystems 16, 4178–4208. doi:10.1002/2015GC006150

Sagong, H., Kwon, S.-T., Ree, J.-H., 2005. Mesozoic episodic magmatism in South Korea and its tectonic implication. Tectonics 24, n/a-n/a. doi:10.1029/2004TC001720

Saleeby, J., Ducea, M., Clemens-Knott, D., 2003. Production and loss of high-density batholithic root, southern Sierra Nevada, California. Tectonics 22. doi:10.1029/2002TC001374

Sarmiento-Rojas, L.F., Van Wess, J.D., Cloetingh, S., 2006. Mesozoic transtensional basin history of the Eastern Cordillera, Colombian Andes: Inferences from tectonic models. J. South Am. Earth Sci. 21, 383–411. doi:10.1016/j.jsames.2006.07.003

Schmidt, M.W., 1992. Amphibole composition in tonalite as a function of pressure: an experimental calibration of the Al-in-hornblende barometer. Contrib. to Mineral. Petrol. 110, 304–310. doi:10.1007/BF00310745

Siégel, C., Bryan, S.E., Allen, C.M., Gust, D.A., 2018. Use and abuse of zircon-based thermometers: A critical review and a recommended approach to identify antecrystic zircons. Earth-Science Rev. 176, 87–116. doi:10.1016/j.earscirev.2017.08.011

Spikings, R., Cochrane, R., Villagomez, D., Van der Lelij, R., Vallejo, C., Winkler, W., Beate, B., 2015. The geological history of northwestern South America: from Pangaea to the early collision of the Caribbean Large Igneous Province (290–75Ma). Gondwana Res. 27, 95–139. doi:10.1016/j.gr.2014.06.004

Spikings, R.A., Cochrane, R., Vallejo, C., Villagomez, D., Van der Lelij, R., Paul, A., Winkler, W., 2019. Latest Triassic to Early Cretaceous tectonics of the Northern Andes: Geochronology, geochemistry, isotopic tracing, and thermochronology, in: Andean Tectonics. Elsevier, pp. 173–208. doi:10.1016/B978-0-12-816009-1.00009-5

Stern, R.J., 2002. Subduction zones. Rev. Geophys. 40, 38. doi:10.1029/2001RG000108

Tindle, A.G., Webb, P.C., 1990. Estimation of lithium contents in trioctahedral micas using microprobe data: application to micas from granitic rocks. Eur. J. Mineral. 2, 595–610. doi:10.1127/ejm/2/5/0595

Villagómez, D., Spikings, R., Magna, T., Kammer, A., Winkler, W., Beltrán, A., 2011. Geochronology, geochemistry and tectonic evolution of the Western and Central cordilleras of Colombia. Lithos 125, 875–896. doi:10.1016/j.lithos.2011.05.003

Wang, R., Tafti, R., Hou, Z., Shen, Z., Guo, N., Evans, N.J., Jeon, H., Li, Q., Li, W., 2017. Across-arc geochemical variation in the Jurassic magmatic zone, Southern Tibet: Implication for continental arc-related porphyry Cu Au mineralization. Chem. Geol. 451, 116–134. doi:10.1016/j.chemgeo.2017.01.010

Whattam, S.A., Stern, R.J., 2016. Arc magmatic evolution and the construction of continental crust at the Central American Volcanic Arc system. Int. Geol. Rev. 58, 653–686. doi:10.1080/00206814.2015.1103668

Winter, J.D., 2014. Principles of Igneous and Metamorphic Petrology, Second edi. ed. Pearson education.

Wörner, G., Mamani, M., Blum-Oeste, M., 2018. Magmatism in the Central Andes.

Elements 14, 237–244. doi:10.2138/gselements.14.4.237

Xie, F., Tang, J., Lang, X., Ma, D., 2018. The different sources and petrogenesis of Jurassic intrusive rocks in the southern Lhasa subterrane, Tibet: Evidence from the trace element compositions of zircon, apatite, and titanite. Lithos 314–315, 447–462. doi:10.1016/j.lithos.2018.06.024

Zapata-García, G., Rodríguez-García, G., Arango-Mejía, M.I., 2017. Petrografía, geoquímica y geocronología de rocas metamórficas aflorantes en San Francisco Putumayo y la vía Palermo-San Luis asociadas a los complejos La Cocha-Río Téllez y Aleluya. Boletín Ciencias la Tierra 48–65. doi:10.15446/rbct.n41.58630

Zapata, S., Cardona, A., Jaramillo, C., Valencia, V., Vervoot, J., 2016. U-Pb LA-ICP-MS Geochronology and geochemistry of Jurassic volcanic and plutonic rocks from the Putumayo region (southern Colombia): Tectonics setting and regional correlations. Boletín Geol. 38, 21–38.

Zhou, L., Wang, R., Hou, Z., Li, C., Zhao, H., Li, X.-W., Qu, W.-J., 2018. Hot Paleocene-Eocene Gangdese arc: Growth of continental crust in southern Tibet. Gondwana Res. 62, 178–197. doi:10.1016/j.gr.2017.12.011

Zhu, D., Wang, Q., Cawood, P.A., Zhao, Z., Mo, X., 2017. Raising the Gangdese Mountains in southern Tibet. J. Geophys. Res. Solid Earth 122, 214–223. doi:10.1002/2016JB013508